On the feasibility of simultaneous identification of a material property of a Timoshenko beam and a moving vibration source★

Bruno Guidio[a], Chanseok Jeong[b,*]

[a]Department of Civil and Environmental Engineering, The Catholic University of America, Washington, DC 20064, USA
[b]School of Engineering and Technology, Central Michigan University, Mount Pleasant, MI 48859, USA

ARTICLE INFO

Keywords:
Joint inversion;
Passive wave source-based structural health monitoring (SHM);
Vehicle-induced ambient vibrations;
Timoshenko beam;
Genetic algorithm (GA);
Finite element method (FEM).

ABSTRACT

This paper presents a computational study for investigating the feasibility of simultaneous identification of a material property of a Timoshenko continuous beam and a moving vibration source on the beam by using the data of measured vibrations on it. This work employs the finite element method to solve the wave equations of a Timoshenko beam subject to a moving vibrational source. It uses the Genetic Algorithm (GA) as an inversion solver to identify the values of targeted control parameters that characterize a material property of the beam and a moving vibration source on it. The numerical results show that, first, the presented inversion method can detect the characteristics of a moving wave source as well as the spatial variation of the elastic modulus of a Timoshenko-beam continuous bridge model, which is set to be piece wisely homogeneous in this work. Second, the GA-based joint inversion is effective even when the moving vibrational source's moving velocity is not constant over time. Third, the detrimental effect of noise in measurement data on the accuracy of the inversion becomes more significant as the number of control parameters increases. By using the presented method, engineers can take advantage of vehicle-induced ambient vibrations on bridges measured by modern sensors for the sake of passive wave source-based structural health monitoring (SHM).

1. Introduction

There is a need to characterize the spatial distributions of the material properties of transportation infrastructures (e.g., a bridge, a tunnel, a roadway, and a railway) and find any anomaly of their material properties (e.g., reduced stiffness caused by corrosion or cracks in their structural members). To this end, engineers employ vibration-based structural health monitoring (SHM) methods by employing active wave sources (e.g., impacts or vibrations) of known signals onto an inspected structure and measuring corresponding vibration responses on it [31]. From those measured vibrations, engineers back-calculate the properties of the structure [5]. There have been theoretical and computational studies for identifying the material properties of a solid structure by using sparsely-measured vibration data induced by active wave sources. For instance, there had been studies on the full-waveform inversion algorithms, based on the partial differential equation (PDE)-constrained optimization, to identify shear modulus profiles of 1D and 2D solids that are truncated by Perfectly-Matched-Layers (PML) by using shear waves [17, 18]. Tran and McVay [32] studied the full-waveform inversion for a 2D solid domain by using the Gauss-Newton method and the finite difference method for solving the elastic wave equation. Pakravan et al. [29] studied the full-waveform inversion for imaging the elastic and attenuating parameters of 2D viscoelastic layered media. Kallivokas et al. [16], Fathi et al. [8], and Fathi et al. [9] had investigated the full-waveform inversion in 2D and 3D elastodynamic, PML-truncated solid domains and validated their numerical studies by using field experimental data. In addition, it had been shown that strong discontinuities within solids, such as the boundaries of cracks or voids, can be identified by using inverse modelings coupled with the boundary element method (BEM) [11, 12] or the extended finite element method (XFEM) [14, 33]. Both BEM and XFEM wave solvers can model the boundaries of the strong discontinuities and update their geometries without cumbersome remeshing during an inversion process as opposed to a conventional finite element method (FEM) wave solver, which should remesh a domain to update the boundaries' geometries. Despite the aforementioned extensive development, as a disadvantage of the active wave source-based SHM approach, it requires traffics on or near an inspected transportation structure to be stopped in order to minimize the random noises in measurement data. It is also

★This document is the results of the research project funded by the National Science Foundation.
*Corresponding author
jeong1c@cmich.edu (C. Jeong)
ORCID(s): 0000-0002-0488-8559 (C. Jeong)

costly to use the active wave source-based SHM approach to infrastructures frequently. Therefore, there is a need to develop its alternative.

In order to seek such an alternative method, this research studies a passive wave source-based SHM approach, by which engineers can take advantage of ambient vibration sources, such as vehicles on roadway or trains on railroads. As an advantage of the passive wave source-based SHM approach, elastic waves, induced by strong vibrational forces (e.g., tractions exerted by moving trailer trucks or trains on an inspected structure), can reach far fields of the structure—including not only the structure but also the soils and foundations under the structure. Thus, the measured data of such waves can carry information about the mechanical properties of infrastructures of large extents. As another advantage of the passive wave source-based SHM approach, engineers can take advantage of unlimited amounts of ambient vibration data from a network of modern, ubiquitous sensors, e.g., fiber optic cables [6], in infrastructures. Namely, because engineers can measure the traffic-induced ambient vibrations on an inspected infrastructure on a day-to-day basis without interrupting its normal operations, they can identify its material properties frequently.

The studies related to the passive wave source-based material characterization are shown in the following. Akcelik et al. [1] simultaneously inverted for a simplified seismic source time signal and material properties in a large 3D truncated domain by using the full-waveform inversion method. Cavadas et al. [4] studied a pattern recognition method that examines vibration data due to regular traffic, to detect wave sources' information and the location of stiffness reduction in a beam, considering only the quasi-static components of vibration responses (instead of their time-domain waveform signals). Liu et al. [23] investigated signal processing and dimensionality-reduction techniques that can identify the relationship between the damage severity of a structure and the vibration responses of a passing vehicle by using mobile sensors installed on a vehicle. Mei et al. [27] presented a theoretical and experimental study for the detection of structural damages using sensors on passing-by vehicles, and considering vehicle-bridge dynamic interaction. Eshkevari et al. [7] presented a structural modal identification method based on data collected by multiple moving sensors (i.e., vehicles), that can lead to frequencies, damping ratios, and high-resolution mode shapes of bridges. Despite the recent development mentioned above, to date, the literature is not mature on the theoretical and computational studies to back-calculate the spatial distributions of material properties of infrastructures by using traffic-induced ambient vibration signals.

To fill this gap, this paper attempts to investigate the feasibility to identify unknown information of (i) the stiffness of a 1D beam bridge model and (ii) a moving wave source on it. When an inverse problem is aimed at identifying the distributions of multiple independent variables (e.g., the simultaneous inversion of the Lamé parameters of a solid [21]), it is known that the inverse problem suffers from solution multiplicity more severely than that aimed at identifying a single variable. Thus, to address the solution multiplicity of the presented joint inversion problem, we employ the Genetic Algorithm (GA), which is known to be a global optimization method for an optimization problem of a small number of control parameters. As a study related to the damage detection using the GA, Mehrjoo et al. [26] proposed a new GA-based method to detect the depth and location of a crack in a structure by analyzing the natural frequencies of the structure extracted from vibrational measurement data. Similarly, Akula and Ganguli [2] investigated a GA-based method to construct a hingeless helicopter rotor blade from its natural frequencies extracted from its vibrational data.

As a structural model, we consider the Timoshenko beam model instead of the Euler-Bernoulli model. We note that the latter does not take into account the effects of shear deformation and rotational inertia of a beam, without which the accuracy of the wave responses of a beam is compromised [3]. Namely, Law and Zhu [22] compared the performance of a moving-force identification method based on both the Timoshenko and Euler-Bernoulli beam theory with respect to various parameters; and they found that, in general, the Timoshenko beam model leads to more accurate results than the other. Because of such accuracy of the Timoshenko beam model, Sarkar and Ganguli [30] considered the Timoshenko beam theory to study higher modes of rotating elastic beams. Khaji et al. [20] also employed the Timoshenko beam model to investigate an analytical method for crack identification in uniform beams.

In this paper, a piece-wisely homogeneous Timoshenko beam is utilized in our parametric studies to test the GA-based joint inversion solver's performance with respect to the number of control parameters, the number of sensors, the population size of the GA, the noise level in measurement data, and the source's moving velocity with/without its acceleration.

2. Problem Definition

This study is aimed at identifying both (i) the spatial distribution of a material property of a Timoshenko continuous beam-based bridge model and (ii) the profile of a moving vibrational source by using the GA-based inverse modeling.

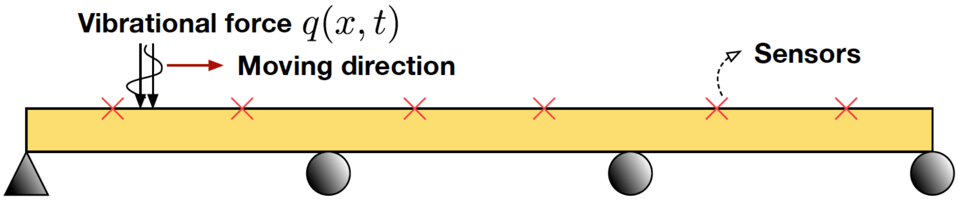

(a) A beam subject to a moving vibrational load

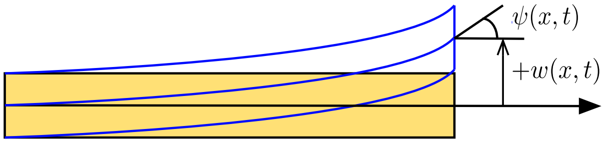

(b) The vertical deflection $w(x,t)$ and slope $\psi(x,t)$ of a beam

Figure 1: Problem configuration.

This work considers a one-dimensional Timoshenko beam supported at four locations by a hinge and rollers (see Fig. 1). Its governing wave equations are the followings [19] (for brevity, the temporal and spatial dependencies of variables are omitted in the following equations):

$$\frac{\partial}{\partial x}\left\{GAK_s\left(\frac{\partial w}{\partial x}-\psi\right)\right\}-\rho A\frac{\partial^2 w}{\partial t^2}=-q, \tag{1}$$

$$GAK_s\left(\frac{\partial w}{\partial x}-\psi\right)+\frac{\partial}{\partial x}\left(EI\frac{\partial \psi}{\partial x}\right)-\rho I\frac{\partial^2 \psi}{\partial t^2}=0, \tag{2}$$

where $x \in (0, L)$ denotes a position in the beam (L is the total length of the beam); $t \in (0, T)$ denotes time (T is the total observation time); $w(x,t)$ is the total vertical deflection of a beam at x and t, and $\psi(x,t)$ is the slope of a beam caused by bending only (see Fig. 1(b)); $E(x)$ is Young's modulus; $G(x)$ is the shear modulus; $\rho(x)$ is the mass density; and $A(x)$ and $I(x)$ denote the cross-sectional area and the second moment of inertia, respectively; $K_s(x)$ denotes the Timoshenko shear factor; and $q(x,t)$ is the excitation force applied from a wave source (e.g., a moving vehicle) on the beam.

The beam is supported at multiple locations by a hinge and rollers, and, hence, the boundary conditions (BCs) of the beam are:

$$w(x=s,t)=0, \quad 0 \le t \le T, \tag{3}$$

$$EI\frac{\partial \psi}{\partial x}(x=s,t)=0, \quad 0 \le t \le T, \tag{4}$$

where s denotes the location of either a hinge or a roller. Equations (3) and (4) indicate that the deflection and the bending moment of the beam vanish at the locations of the hinge and roller supports. The beam is initially at rest: the initial-value conditions are:

$$w(x,0)=0, \quad \frac{\partial w}{\partial t}(x,0)=0, \tag{5}$$

$$\psi(x,0)=0, \quad \frac{\partial \psi}{\partial t}(x,0)=0. \tag{6}$$

This paper considers that there is a moving vibrational force exerted on the beam. Namely, the vibrational force in (1) is defined as:

$$q(x,t)=F(t)H(x,t), \tag{7}$$

where the time-harmonic excitation of the force is defined as:

$$F(t)=-P\sin(2\pi f t), \tag{8}$$

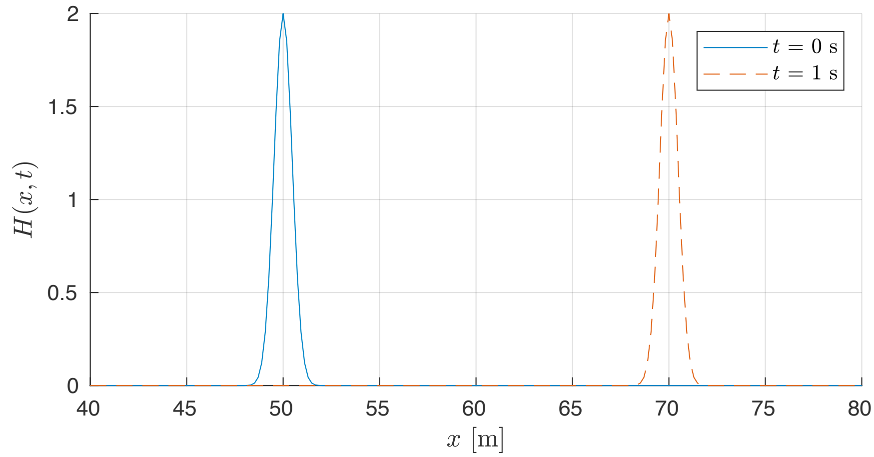

Figure 2: Two snapshots of $H(x,t)$ at, respectively, $t = 0$ and 1 s using $x_0 = 50$ m and $\vartheta = 20$ m/s.

where P is the amplitude of the sinusoidal temporal variation of the force; f is its frequency. In (7), the time-dependent (i.e., moving) spatial variation term, i.e., $H(x,t)$ of $q(x,t)$ is defined as:

$$H(x,t) = (\cos(z) + 1)\mathrm{e}^{(-|2\times z^2|)}, \quad z = x - x_0 - \vartheta t, \tag{9}$$

where x_0 denotes the position of the centroid of $H(x,t)$ at the initial observation time ($t = 0$); and ϑ is its moving speed (please see an example of the snapshots of $H(x,t)$ in Fig. 2). We note that $H(x,t)$ represents the spatial function of a moving wave source with a single contact area where traction is applied as the Gaussian distribution [24].

In this study, the values of the amplitude P and frequency f of $F(t)$ are unknown and set to be reconstructed while the initial position x_0 and moving speed ϑ of $H(x,t)$ are known during the presented inversion solver. Thus, we would like to remark that the presented method is a partially-passive SHM approach. Here, we consider that, in practice, engineers can easily estimate x_0 and ϑ by using visual footage made by traffic-surveillance cameras and transfer the known information of x_0 and ϑ to the inversion solver.[1] In contrast, the amplitude P and f are hard to estimate from the video footage because P is affected by the total weight of a vehicle, including its passengers and freights, and f is associated with the vehicle's internal vibration. Thus, this work aims to identify P and f of a wave source as well as the material property of a beam.

3. Forward Wave Modeling

This section presents the finite element modeling for obtaining the numerical solutions of the governing wave equations (1) and (2).

3.1. Finite Element Method

The governing wave equations (1) and (2) are multiplied by test functions $u(x)$ and $v(x)$, respectively, and integrated over the domain $(0, L)$. Then, they become the following weak forms:

$$-\int_0^L \left(GAK_s \frac{\partial w}{\partial x}\frac{\partial u}{\partial x}\right) \mathrm{d}x + \int_0^L \left(GAK_s \psi \frac{\partial u}{\partial x}\right) \mathrm{d}x - \int_0^L \left(\rho A u \frac{\partial^2 w}{\partial t^2}\right) \mathrm{d}x = -\int_0^L (uq)\, \mathrm{d}x, \tag{10}$$

$$\int_0^L \left(GAK_s v \frac{\partial w}{\partial x} - GAK_s v\psi\right) \mathrm{d}x - \int_0^L \left(EI \frac{\partial v}{\partial x}\frac{\partial \psi}{\partial x}\right) \mathrm{d}x - \int_0^L \left(\rho I v \frac{\partial^2 \psi}{\partial t^2}\right) \mathrm{d}x = 0. \tag{11}$$

[1] Please note that engineers can choose to use the data made during a particular observation time (e.g., midnight), when there is only a single vehicle on an inspected bridge, for the presented inversion solver. From the vibrational data that are obtained during such a time slot, we invert for the control parameters of only one wave source and the material properties of an inspected structure. Joint inversion is more plausible to solve in a case with only one unknown wave source than a case with multiple unknown sources: the more control parameters are to be inverted for, an inverse problem is more likely to suffer from the solution multiplicity.

Next, the test and trial functions are approximated as follows:

$$\begin{aligned} u(x) &\simeq \mathbf{u}^T \boldsymbol{\phi}(x), \quad v(x) \simeq \mathbf{v}^T \mathbf{g}(x), \\ w(x,t) &\simeq \boldsymbol{\phi}(x)^T \mathbf{w}(t), \quad \psi(x,t) \simeq \mathbf{g}(x)^T \boldsymbol{\Psi}(t), \end{aligned} \tag{12}$$

where $\mathbf{w}(t)$ and $\boldsymbol{\Psi}(t)$ are the vectors of unknown nodal deflections and slopes of a beam, respectively, and $\boldsymbol{\phi}(x)$ and $\mathbf{g}(x)$ are the vectors of global basis functions that are made of shape functions in the local coordinate of each element. In this work, we use the Lagrange 4-noded cubic shape functions to approximate $w(x,t)$ and $u(x)$, and the Lagrange 3-noded quadratic shape functions to approximate $\psi(x,t)$ and $v(x)$ [19].

By virtue of the approximation of the test and trial functions as shown in (12), the weak form (10) and (11) reduce to the following semi-discrete system:

$$\mathbf{M}\ddot{\mathbf{d}}(t) + \mathbf{K}\mathbf{d}(t) = \mathbf{Q}(t), \tag{13}$$

where $(\ddot{\ })$ denotes the second-order derivative of a subtended variable with respect to t; $\mathbf{M}$ denotes a global mass matrix; $\mathbf{K}$ denotes a global stiffness matrix; $\mathbf{Q}$ denotes a global load vector; and $\mathbf{d}(t)$ is the solution vector composed by $\mathbf{w}(t)$ and $\boldsymbol{\Psi}(t)$. In (13), the vectors and matrices are defined as:

$$\mathbf{d}(t) = \begin{bmatrix} \mathbf{w}(t) \\ \boldsymbol{\Psi}(t) \end{bmatrix}, \quad \mathbf{Q}(t) = \begin{bmatrix} -\int_0^L \boldsymbol{\phi} q \, \mathrm{d}x \\ \mathbf{0} \end{bmatrix}, \tag{14}$$

$$\mathbf{M} = \begin{bmatrix} \int_0^L \rho A \boldsymbol{\phi}\boldsymbol{\phi}^T \, \mathrm{d}x & \mathbf{0} \\ \mathbf{0} & \int_0^L \rho I \mathbf{g}\mathbf{g}^T \, \mathrm{d}x \end{bmatrix}, \tag{15}$$

$$\mathbf{K} = \begin{bmatrix} \int_0^L GAK_s \boldsymbol{\phi}' \boldsymbol{\phi}'^T \, \mathrm{d}x & \int_0^L GAK_s \boldsymbol{\phi}' \mathbf{g}^T \, \mathrm{d}x \\ \int_0^L GAK_s \mathbf{g} \boldsymbol{\phi}'^T \, \mathrm{d}x & \int_0^L (GAK_s \mathbf{g}\mathbf{g}^T + EI\mathbf{g}'\mathbf{g}'^T) \, \mathrm{d}x \end{bmatrix}, \tag{16}$$

where $(\,'\,)$ denotes the derivative of a subtended variable with respect to x.

We solve the time-dependent ordinary differential equation (13) in every i-th discrete time step as:

$$\mathbf{M}\ddot{\mathbf{d}}_i + \mathbf{K}\mathbf{d}_i = \mathbf{Q}_i. \tag{17}$$

By applying the initial-value conditions (5) and (6) onto (17), the solution vector at the initial time step is obtained by solving the following:

$$\mathbf{M}\ddot{\mathbf{d}}_1 = \mathbf{Q}_1. \tag{18}$$

After the initial time step, this work solves the system of equation for each time step using Newmark implicit time integration (i.e., the average acceleration scheme), which results in the unconditionally-stable numerical solution of wave responses [28]. The solution vector of the i-th time step is related to its previous time step as:

$$\mathbf{d}_i = \mathbf{d}_{i-1} + \dot{\mathbf{d}}_{i-1}(\Delta t) + \frac{1}{2}[0.5\ddot{\mathbf{d}}_{i-1} + 0.5\ddot{\mathbf{d}}_i](\Delta t)^2, \tag{19}$$

and

$$\dot{\mathbf{d}}_i = \dot{\mathbf{d}}_{i-1} + [0.5\ddot{\mathbf{d}}_{i-1} + 0.5\ddot{\mathbf{d}}_i](\Delta t), \tag{20}$$

where Δt denotes the size of a time step. By plugging (19) into (17), it turns into the following:

$$[\mathbf{M} + 0.25\mathbf{K}(\Delta t)^2]\ddot{\mathbf{d}}_i = \mathbf{Q}_i - \mathbf{K}[\mathbf{d}_{i-1} + \dot{\mathbf{d}}_{i-1}(\Delta t) + 0.25\ddot{\mathbf{d}}_{i-1}(\Delta t)^2]. \tag{21}$$

By using (21), this work solves for $\ddot{\mathbf{d}}_i$. Then, the values of $\mathbf{d}_i$ and $\dot{\mathbf{d}}_i$ can be updated by using, respectively, (19) and (20).

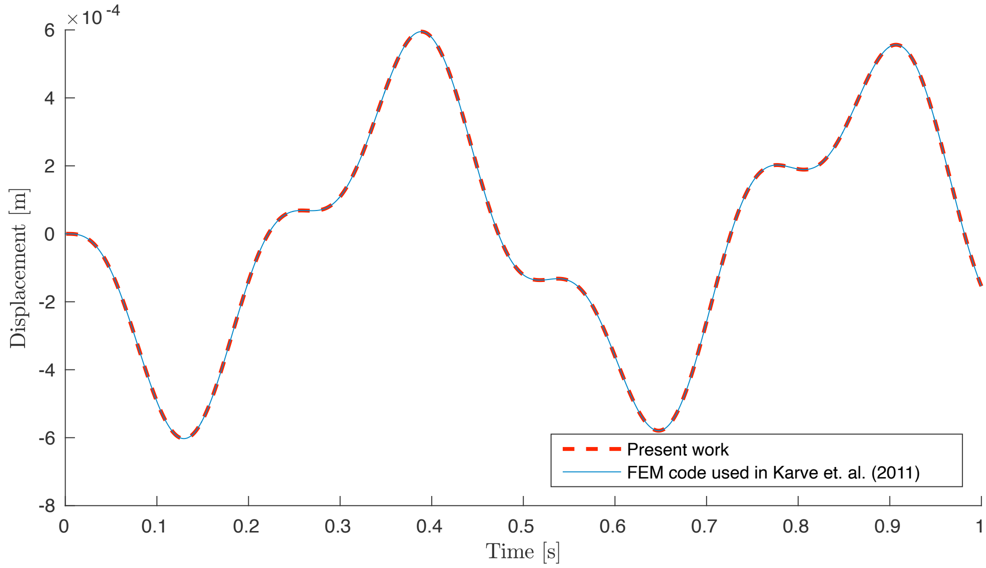

Figure 3: Comparison between $w(5,t)$ generated by our FEM wave solver and that by a reference code for a simply-supported beam of its length 10 m subject to a uniformly-distributed sinusoidal loading of its frequency 2 Hz.

3.2. Verification of the forward wave modeling

Prior to our investigation on the performance of the presented joint inversion, we verify our FEM wave solver, written in MATLAB, by comparing our solution with the reference solution calculated by another wave solver, written in Fortran, used for a previous Timoshenko-beam model-based study by Karve et al. [19]. This verification considers a 10 m-long Timoshenko beam, which is simply supported by a hinge and a roller. The beam is discretized by using 100 elements (each element is 0.1 m long), and the total observation duration T is 1.0 s with a time step Δt of 0.001 s. The beam is homogeneous and has the following properties: Young's modulus (E) of 2.5×10^{10} Pa, shear modulus (G) of 1×10^{10} Pa, mass density (ρ) of 2500 kg/m^3, cross-section area (A) of 0.1 m^2, second moment of inertia (I) of 0.0013 m^4, and shear factor (K_s) of 0.8333. In this verification, a uniformly-distributed excitational loading is exerted on all the elements of the beam, and it is defined as $q(x,t) = 100\sin(2\pi f t)$ N/m with its frequency f of 2 Hz. Fig. 3 shows an excellent agreement between the displacement field of the wave response, in the center of the beam, from our FEM wave solver and that from the reference code. Hence, the forward wave modeling presented in this work is reliable and can be used in the presented inversion modeling.

4. Inverse Modeling

The objective of the inverse modeling in this work is to estimate the values of the control parameters—characterizing a moving wave source and the spatial distribution of a material property of a beam—that minimize the following misfit functional:

$$\mathcal{L} = \int_0^T \sum_{j=1}^{\mathrm{NS}} (w_j^{\mathrm{m}}(t) - w_j(t))^2 \,\mathrm{d}t. \tag{22}$$

In (22), T is the total observation time; NS is the number of sensors; w_j^{m} and w_j are, respectively, the measured wave response of the deflection, due to targeted control parameters, and its computed counterpart, due to estimated parameters, at the location of the j-th sensor and time t. In this computational study, we synthetically create the measured response data, $w_j^{\mathrm{m}}(t)$, by using our FEM solver with targeted control parameters. To avoid an inverse crime, the element size used for computing $w^{\mathrm{m}}(t)$ is half the size of that for $w(t)$. The misfit functional (22) is of a L^2 norm (the square of the difference between $w_j^{\mathrm{m}}(t)$ and $w_j(t)$), which is considered to increase the misfit functional value of outliers exponentially [13, 15, 17, 21].

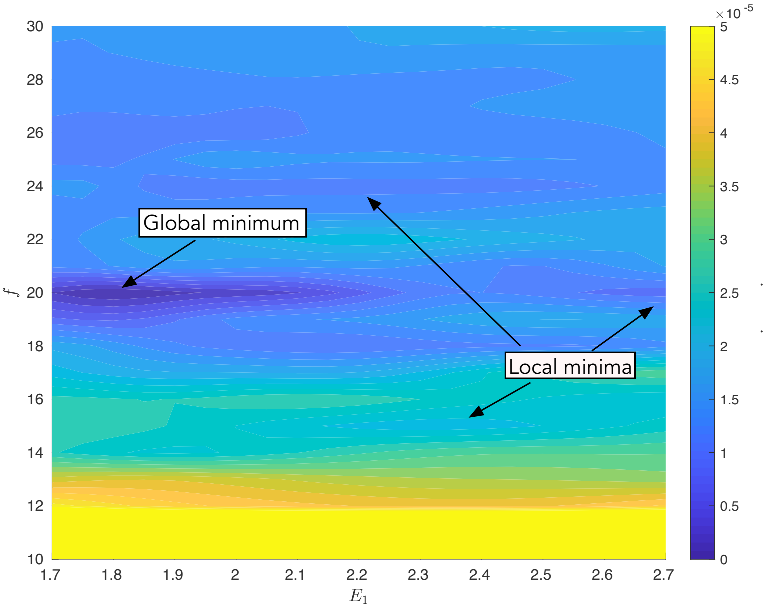

Figure 4: An exemplary contour plot of the objective functional with respect to two control parameters.

In this work, the Genetic Algorithm (GA) is employed to estimate unknown values of control parameters that correspond to the minimal value of the misfit functional (22). We choose to use the GA because of its effectiveness for an optimization or inverse problem with respect to a small number of control variables—in our presented numerical experiments, the number of control parameters is sufficiently small (e.g., five in Example 1-2, six in Example 3, eleven in Example 4-5, and twelve in Example 6). We also chose to use the GA because it is known to be an effective method to identify control parameters that correspond to the global minimum (or a local minimum that is closer to the global minimum than other local minima) of an objective functional. Fig. 4 presents an anecdoctal evidence, supporting that the objective functional of the presented joint inversion problem has a number of local minima. Namely, the contour plot in Fig. 4 shows the distribution of the objective functional with respect to estimated values of E_1 and f in Example 1 shown in Section 5.1 (please note that the estimated values of E_2, E_3 and A are the same as their targeted counterparts in Example 1 only for showing this contour plot).

The GA involves a series of generations (i.e., inversion iterations). At each generation, the GA explores the profiles of a given number of individuals, each of which contains a set of all the control parameters. Namely, in the presented inverse modeling, each individual consists of following control parameters—the amplitude and frequency of a moving wave source and the Young's modulus of each segment in a Timoshenko beam model, which is assumed to be piece wisely homogeneous.

The total number of generations is referred to as GN in this paper. In the beginning of the GA, it is assigned the value of GN and a given number of individuals, which is referred to as the population size (PS). As mutation and cross-over among the individuals diversify each population, the GA explores the fittest individual. At the last generation, the GA returns the fittest individual that leads to the smallest value of the misfit functional, and its control parameters will be the final inversion solution. This work uses the built-in GA function in MATLAB, and it autonomously conducts the mutation and cross-over of individuals, for each of which $w_j(t)$ at each j-th measurement location is computed by using our forward wave solver.

5. Numerical Experiments

This section shows six numerical examples, investigating the performance of the presented GA-based joint inversion method with respect to various factors. The first example is focused on the performance of the presented inversion solver for estimating the values of five control parameters—two for a moving source and three for the elastic moduli of the beam structure's three segments. The second example tests the inversion performance of reconstructing the values of five control parameters with respect to the noise level. The third example shows the capability of our inverse modeling to reconstruct six control parameters—three for a moving source, of which moving speed varies over time, and three for the elastic moduli of beam structure's three segments. The fourth example examines the inversion solver for estimating the values of eleven control parameters—two for a moving source and nine for the elastic moduli of the beam structure's nine segments. The fifth example investigates the performance of reconstructing the values of eleven control parameters with respect to the noise level. Lastly, the sixth example tests the performance of the presented GA-based joint inversion solver for estimating twelve control parameters—three source parameters and nine structural parameters—by considering that the velocity of the moving source is not constant over time. In these six examples, this work investigates the effects of the population size (PS) and/or the number of sensors (NS) on the performance of the presented joint inversion algorithm.

In all the examples, we consider a Timoshenko beam bridge model, of which the total extent is 100 m. It is supported by a hinge at x of 0 m, and three rollers at x of 33.3, 66.7, and 100 m, respectively. When we compute $w_j(t)$, the beam is discretized by using 180 elements (an element size is about 0.56 m, and each element contains a set of 4 nodes for approximating w and another set of 3 nodes for approximating Ψ), and the time step of 0.001 s is used in the FEM solver. The total observation duration T is 1.0 s, and the sensors are sparsely distributed along the beam with uniform spacing.

In the presented inversion simulations, it is assumed that the inversion solver uses the following *a-priori* known, uniformly-distributed material properties of a beam —ρ of 2500 kg/m^3, A of 0.1 m^2, I of 0.0013 m^4, and K_s of 0.8333. On the other hand, the value of E is unknown, and it could vary with respect to the location of the beam model. Thus, its spatial distribution is to be identified during the inverse modeling. In the presented numerical examples of the joint inversion, a targeted moving wave source is known to move with its moving speed ϑ of 20 m/s toward the right-hand side of the beam from its initial position at x_0 of 50 m. In contrast, its amplitude (P) of 100 N/m and frequency (f) of 20 Hz are unknown, and their values will be reconstructed during the presented GA process while the upper and lower limits of P and f are set by using ± 50% deviations of their targeted values. That is, their values are bounded as $50 \leq P \leq 150$ N/m and $10 \leq f \leq 30$ Hz during the presented inversion process.

As the postprocessing of the inversion results, the error between each target control parameter and its corresponding estimated solution of the fittest individual at each generation is computed as:

$$\mathcal{E} = \frac{|\text{A targeted value} - \text{An estimated value from the GA}|}{|\text{A targeted value}|} \times 100\,[\%]. \tag{23}$$

An averaged error norm for all the control parameters of the fittest individual at each generation is also defined as:

$$\overline{\mathcal{E}} = \frac{\sum_{k=1}^{\text{NP}} \mathcal{E}_k}{\text{NP}}\,[\%]. \tag{24}$$

where NP denotes the total number of target control parameters of an individual, and k denotes the k-th control parameter of an individual, and $\mathcal{E}_k$ is the error, defined in (23), of the inversion of the k-th control parameter.

5.1. Example 1 (Cases 1 to 5): joint inversion of two source parameters and three stiffness parameters in a bridge comprised of three piece wisely-homogeneous segments

In this example, we consider that a continuous beam model consists of three piece wisely-homogeneous segments (see Fig. 5), and each segment's Young's modulus (E) is estimated by the presented joint inversion method. The targeted value of E_1 of the beam's first segment ($0 \leq x \leq 33.3$ m) is 1.8×10^{10} Pa, and it is smaller than those (E_2 and E_3 of 2.5×10^{10} Pa) of the other segments ($33.3 \leq x \leq 100$ m). This reduced stiffness in the first segment represents a structural anomaly, e.g., corrosion-induced reduced stiffness.

Fig. 6 shows the snapshots of a targeted moving source function $q(x,t)$ and its corresponding wave responses of a displacement field in the entire beam at 0.28 and 0.82 seconds, considering the targeted parameters of the source and the material of this example. Fig. 7 shows the frequency contents of wave responses (up to t of 0.3 s) measured at sensors that are located, respectively, in front of ($x = 60$ m) and behind ($x = 40$ m) the targeted moving source whose excitational frequency is 20 Hz. The wave response, measured at x of 60 m, shows the forward frequency shift (i.e., 20 Hz shifted to 20.31 Hz) of its dominant frequency, and the other, at x of 40 m, shows the backward frequency shift (i.e., 20 Hz shifted to 19.03 Hz). The frequency shifts are attributed to the Doppler effect of the wave responses induced by a moving source [25].

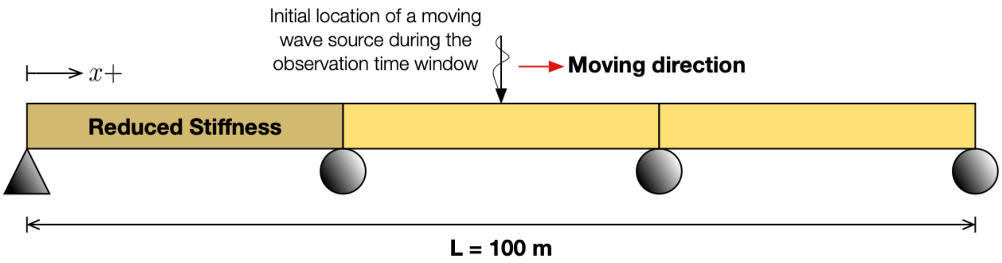

Figure 5: A piece wisely-homogeneous Timoshenko beam with three segments in Example 1, 2, and 3.

Table 1
Example 1: joint inversion of two source parameters and three stiffness parameters in a bridge comprised of three piece wisely-homogeneous segments (GN = 50 for all the cases 1 to 5). The first row shows the targeted control parameters. The second to the sixth rows show their reconstructed values and corresponding errors.

Cases	Parameters	Value	Error, $\mathcal{E}$	Average Error, $\overline{\mathcal{E}}$
Target	P (N/m)	100		
	f (Hz)	20		
	E_1 (Pa)	1.8×10^{10}		
	E_2 (Pa)	2.5×10^{10}		
	E_3 (Pa)	2.5×10^{10}		
Case 1	P (N/m)	99.97	0.0%	0.0 %
$PS = 100$	f (Hz)	20.01	0.0%	
$NS = 45$	E_1 (Pa)	1.80×10^{10}	0.0%	
	E_2 (Pa)	2.50×10^{10}	0.1%	
	E_3 (Pa)	2.50×10^{10}	0.0%	
Case 2	P (N/m)	100.01	0.0%	0.3%
$PS = 50$	f (Hz)	20.01	0.1%	
$NS = 45$	E_1 (Pa)	1.79×10^{10}	0.4%	
	E_2 (Pa)	2.51×10^{10}	0.5%	
	E_3 (Pa)	2.49×10^{10}	0.5%	
Case 3	P (N/m)	100.19	0.2%	0.4%
$PS = 50$	f (Hz)	20.01	0.0%	
$NS = 30$	E_1 (Pa)	1.80×10^{10}	0.1%	
	E_2 (Pa)	2.52×10^{10}	0.6%	
	E_3 (Pa)	2.48×10^{10}	0.9%	
Case 4	P (N/m)	98.81	1.2%	0.4%
$PS = 50$	f (Hz)	20.00	0.0%	
$NS = 15$	E_1 (Pa)	1.80×10^{10}	0.1%	
	E_2 (Pa)	2.51×10^{10}	0.4%	
	E_3 (Pa)	2.49×10^{10}	0.3%	
Case 5	P (N/m)	100.84	0.8%	0.7%
$PS = 50$	f (Hz)	20.01	0.1%	
$NS = 10$	E_1 (Pa)	1.79×10^{10}	0.4%	
	E_2 (Pa)	2.53×10^{10}	1.1%	
	E_3 (Pa)	2.47×10^{10}	1.0%	

The value of the estimated E_n in each n-th segment of the beam is bounded as 1.7×10^{10} Pa $\leq E_n \leq 2.6 \times 10^{10}$ Pa during the GA-based inversion simulation. Please note that E_n is quite unlikely to exceed its designed value of 2.5×10^{10} Pa during the lifespan of a bridge whereas it could become smaller than its designed value due to structural damage.

In this Example 1, Cases 1 to 5 are examined to detect the targeted control parameters by using five different combinations of PS and NS, and we used GN of 50 for all Cases 1 to 5. Both Cases 1 and 2 use NS of 45 (the spacing between neighboring sensors is about 2.2 m), but each of them uses PS of 100 and 50, respectively. On the other hand, Cases 3 to 5 use PS of 50, but each of them uses NS of 30, 15, and 10, respectively (the sensor spacings are 3.3, 6.3, and 9.2 m, respectively, in Cases 3 to 5). Table 1 shows the reconstructed values of the control parameters of the best-fit individual at the final generation in Cases 1 to 5. The table also shows the error $\mathcal{E}$, defined in (23), between the reconstructed value of each parameter and its targeted value and the average error $\overline{\mathcal{E}}$, defined in (24), of all the parameters.

Cases 2 to 5 demonstrate the performance of the inversion solver with respect to the number of sensors (or NS). Namely, as shown in Fig. 8, the average error for the best-fit individual at the final generation tends to increase as NS decreases (e.g., $\overline{\mathcal{E}}$ is 0.3 for PS of 50 and NS of 45 while $\overline{\mathcal{E}}$ is 0.7 for PS of 50 and NS of 10). Table 1 shows that Case 1 results in the smallest average error ($\overline{\mathcal{E}}$ of 0.0%) because Case 1 uses larger values of PS and NS than the other cases.

In this paragraph, we describe the inversion performance of Case 1, which shows the smallest value of $\overline{\mathcal{E}}$ among Cases 1 to 5. Fig. 9 shows how the value of the misfit functional for the best-fit individual changes over the GA iterations in Case 1. Figs. 10 and 11 show the histograms of estimated control parameters of all the individuals during the entire generations in the GA inversion for Case 1. Fig. 10 presents that (*i*) first, the estimated values of parameters P and f of the entire individuals have wide ranges of values (i.e., within the 50% deviations of their targeted values) in the early generations; (*ii*) after the first 15 generations and until the 40-th generation, their values approach to their targeted values (i.e., within the 5% deviations of their targeted values); and, (*iii*) lastly, their variations become significantly low (i.e., within the 1% deviations of their targeted values) during the last 10 generations. The histograms of the structural parameters in the three segments are shown in Fig. 11. It shows the excellent convergence of the estimated values of E_2 and E_3 in the first 20 generations. In contrast, the convergence of the estimated values of E_1 is much slower than those of E_2 and E_3. Nevertheless, our GA-based optimizer successfully updates the estimated value of E_1 such that it converges toward its targeted value with quite a small averaged error (e.g., $\mathcal{E} = 0.0\%$) as shown in Table 1. Lastly, Fig. 12 shows that the wave response, w^{m}, due to the targeted control parameters is in an excellent agreement with w due to the reconstructed ones at two sensors located at x of, respectively, 40 and 60 m.

5.2. Example 2 (Cases 6 to 10): investigating the joint inversion performance of two source parameters and three stiffness parameters with respect to the noise level

This example studies the performance of reconstructing control parameters with respect to the noise level of random noise that is added to w^{m} before inversion. We employed the same continuous beam model presented in Fig. 5, where the first segment has a reduced stiffness. In addition to the Case 1 in Example 1, where the noise level of 0% is used, we considered Cases 6-10, which use noise level of 1%, 5%, 10%, 15%, and 20%, respectively.

Fig. 13 shows w^{m} with 0% noise level (Case 1) and w^{m} with 10% noise level (Case 8) at a sensor at $x = 60$ m. As shown in Table 2 and Fig. 14, the averaged error $\overline{\mathcal{E}}$ of all the Cases 6-10 with noise are about the same (0.1 %). Namely, we found that the inversion performance is not sensitive to the noise level because the number of the control parameters is quite small under this example.

5.3. Example 3 (Cases 11 to 13): joint inversion of three source parameters, including the acceleration of a moving source, and three stiffness parameters

In this example, we consider the same continuous beam model with three piece wisely-homogeneous segments shown in Fig. 5. Similary to Examples 1 and 2, the targeted value of E_1 (1.8×10^{10} Pa) is smaller than those of the other two segments (2.5×10^{10} Pa), and the initial velocity (ϑ) of 20 m/s is known prior the inversion. However, in contrast to Examples 1 and 2, the moving velocity of the moving vibrational source is not considered to be constant over time in this example. Therefore, the variable z in (9) is modified as:

$$z = x - x_0 - \vartheta t - 0.5 a t^2 \tag{25}$$

where a is the acceleration of the spatial variation term $H(x, t)$ of a wave source, and in addition to the other source parameters (P and f), a is set to be estimated under this example. Accordingly, the targeted value of a is 3 m/s^2, and the value of the estimated a is bounded as 1.5 m/s$^2 \leq a \leq$ 4.5 m/s^2 during the inversion.

This example considers Cases 11 to 13, which are evaluated by using PS of 50, 100, and 200, respectively, while all of them use NS of 45 and GN of 50. Table 3 shows the estimated values of control parameters of the best-fit individual at the final generation, the error between the estimated and targeted values, and the average error of all six control parameters in each case.

Table 2
Example 2: Investigating the joint inversion performance with respect to the noise level in a bridge comprised of three piece wisely-homogeneous segments by using NS of 45, GN of 50, and PS of 100.

Cases	Parameters	Value	Error, $\mathcal{E}$	Average Error, $\overline{\mathcal{E}}$
Case 1 Noise level = 0%	P (N/m)	99.97	0.0%	0.0 %
	f (Hz)	20.01	0.0%	
	E_1 (Pa)	1.80×10^{10}	0.0%	
	E_2 (Pa)	2.50×10^{10}	0.1%	
	E_3 (Pa)	2.50×10^{10}	0.0%	
Case 6 Noise level = 1%	P (N/m)	100.36	0.4%	0.1%
	f (Hz)	20.00	0.0%	
	E_1 (Pa)	1.80×10^{10}	0.0%	
	E_2 (Pa)	2.50×10^{10}	0.1%	
	E_3 (Pa)	2.50×10^{10}	0.0%	
Case 7 Noise level = 5%	P (N/m)	100.15	0.2%	0.1%
	f (Hz)	20.00	0.0%	
	E_1 (Pa)	1.80×10^{10}	0.2%	
	E_2 (Pa)	2.50×10^{10}	0.1%	
	E_3 (Pa)	2.49×10^{10}	0.1%	
Case 8 Noise level = 10%	P (N/m)	99.77	0.2%	0.1%
	f (Hz)	20.01	0.0%	
	E_1 (Pa)	1.79×10^{10}	0.1%	
	E_2 (Pa)	2.49×10^{10}	0.2%	
	E_3 (Pa)	2.50×10^{10}	0.0%	
Case 9 Noise level = 15%	P (N/m)	100.04	0.0%	0.1%
	f (Hz)	20.00	0.0%	
	E_1 (Pa)	1.80×10^{10}	0.1%	
	E_2 (Pa)	2.50×10^{10}	0.1%	
	E_3 (Pa)	2.50×10^{10}	0.1%	
Case 10 Noise level = 20%	P (N/m)	100.20	0.2%	0.1%
	f (Hz)	20.01	0.0%	
	E_1 (Pa)	1.80×10^{10}	0.0%	
	E_2 (Pa)	2.51×10^{10}	0.3%	
	E_3 (Pa)	2.49×10^{10}	0.2%	

In all the Cases, the GA-based optimizer is able to identify the segment with the reduced stiffness. In addition, as the population size increases, the error between the estimated and targeted acceleration decreases, i.e., from 14.1% (Case 11 using PS of 50) to 1.3% (Case 13 using PS of 200). Table 3 and Fig. 15 also show that the final value of $\overline{\mathcal{E}}$ for the best-fit individual decreases as the population size increases. Therefore, our optimizer is able to successfully identify the targeted control parameters although the moving velocity of a moving wave source varies over time.

5.4. Example 4 (Cases 14 to 17): joint inversion of two source parameters and nine stiffness parameters in a bridge comprised of nine piece wisely-homogeneous segments

This example considers a continuous beam, which consists of nine piece wisely-homogeneous segments (see Fig. 16). The source parameters and structural parameter values are estimated by our joint inversion solver. In this example, as the targeted stiffness parameter of the beam, E_6 in the sixth segment (1.8×10^{10} Pa) is smaller than those of the other segments (E_1 to E_9, except for E_6, of 2.5×10^{10} Pa). Similarly to Example 1, the estimated value of E_n in each n-th segment of the beam is bounded as $1.7 \times 10^{10} \le E \le 2.6 \times 10^{10}$ Pa during the GA-based inversion simulation.

This example tests Cases 14 to 17, which are evaluated by using PS of 50, 100, 200, and 400, respectively, while all of them use NS of 45 with the sensor spacing of 2.2 m and GN of 50. Table 4 shows the reconstructed source parameter values, the error between their reconstructed and targeted values, and the average error of all the eleven control parameters in each case. The spatial distribution of the recovered stiffness of all the segments in each case is shown in Fig. 17. It presents that the discrepancy between the reconstructed and targeted values of stiffness parameters is decreased as PS is increased. Fig. 18 shows that the values of $\mathcal{L}$ and $\overline{\mathcal{E}}$ for the best-fit individual in each case become

Table 3
Example 3: joint inversion of three source parameters and three stiffness parameters in a bridge comprised of three piece wisely-homogeneous segments (NS =45 and GN = 50 for all the cases 11 to 13). The first row shows the targeted control parameters. The second to the third rows show their reconstructed values and corresponding errors.

Cases	Parameters	Value	Error, $\mathcal{E}$	Average Error, $\overline{\mathcal{E}}$
Target	P (N/m)	100		
	f (Hz)	20		
	a (m/s^2)	3		
	E_1 (Pa)	1.8×10^{10}		
	E_2 (Pa)	2.5×10^{10}		
	E_3 (Pa)	2.5×10^{10}		
Case 11 $PS = 50$	P (N/m)	101.44	1.4%	3.0%
	f (Hz)	20.01	0.0%	
	a (m/s^2)	3.42	14.1%	
	E_1 (Pa)	1.80×10^{10}	0.0%	
	E_2 (Pa)	2.47×10^{10}	1.4%	
	E_3 (Pa)	2.53×10^{10}	1.2%	
Case 12 $PS = 100$	P (N/m)	100.63	0.6%	1.6%
	f (Hz)	20.02	0.1%	
	a (m/s^2)	3.22	7.4%	
	E_1 (Pa)	1.79×10^{10}	0.4%	
	E_2 (Pa)	2.51×10^{10}	0.5%	
	E_3 (Pa)	2.48×10^{10}	0.7%	
Case 13 $PS = 200$	P (N/m)	100.09	0.1%	0.3%
	f (Hz)	20.01	0.0%	
	a (m/s^2)	2.96	1.3%	
	E_1 (Pa)	1.81×10^{10}	0.3%	
	E_2 (Pa)	2.50×10^{10}	0.1%	
	E_3 (Pa)	2.50×10^{10}	0.0%	

smaller as the generation approaches to the last one. It also clearly shows the improvement of the accuracy of the joint inversion as we increase PS.

5.5. Example 5 (Cases 18 to 20): investigating the joint inversion performance of two source parameters and nine stiffness parameters with respect to the noise level

In this example, we focus on examining the performance of reconstructing eleven control parameters with respect to the noise level of random noise added to w^{m}. We used the piece wisely-homogeneous Timoshenko beam with nine segments, shown in Fig. 16, in consideration of NS of 45, GN of 50, and PS of 400. In addition to 0% of noise, utilized in Case 17 in Example 4, we examined the noise level of 1%, 10%, and 20%, which correspond to Cases 18-20, respectively.

Table 5 summarizes the results of the critical control parameters, while Fig. 19 shows the comparisons among all the targeted and estimated stiffness control parameters in each case. In example 3, the inversion performance is not sensitive to the noise level due to the small number of control parameters. However, in this example, where eleven control parameters are to be identified, the larger noise level leads to the larger error for the final best fit-individual in each case as shown in Table 5 and Fig. 20. Thus, we suggest that the detrimental effect of noise in measurement on the inversion accuracy increases as the number of control parameters increases.

5.6. Example 6 (Case 21): joint inversion of three source parameters, including the acceleration of a moving source, and nine stiffness parameters

This example considers the same continuous beam utilized in examples 4 and 5, a piece wisely-homogeneous beam with nine segments. However, unlike examples 4 and 5, this example considers that the source parameter's velocity is not constant over time. Namely, this example attempts to identify three source parameters — P, f, and a. Therefore, similar to Example 3, the variable z in (9) is modified to that in (25).

Table 4
Example 4 - joint inversion of two source parameters and nine stiffness parameters in a bridge comprised of nine piece wisely-homogeneous segments by using NS of 45, GN of 50, and PS of different values: while only the key control parameters are shown in this table, all the stiffness control parameters are visualized in Fig. 17. The first row shows the targeted control parameters of P, f, and E_6. The second to the fifth rows show their reconstructed values, individual errors, and averaged errors.

Cases	Key Control Parameters	Value	$\mathcal{E}$ (only P, f, E_6)	$\overline{\mathcal{E}}$ (only E_1 to E_9)	$\overline{\mathcal{E}}$
Target	P (N/m)	100			
	f (Hz)	20			
	E_6 (Pa)	1.80×10^{10}			
Case 14 $PS = 50$	P (N/m)	99.09	0.9%	3.8%	3.2%
	f (Hz)	20.01	0.1%		
	E_6 (Pa)	1.93×10^{10}	6.9%		
Case 15 $PS = 100$	P (N/m)	100.45	0.5%	3.5%	2.9%
	f (Hz)	20.01	0.1%		
	E_6 (Pa)	1.98×10^{10}	10.2%		
Case 16 $PS = 200$	P (N/m)	99.12	0.9%	1.8%	1.5%
	f (Hz)	20.01	0.0%		
	E_6 (Pa)	1.87×10^{10}	3.7%		
Case 17 $PS = 400$	P (N/m)	99.66	0.3%	1.0%	0.8%
	f (Hz)	20.00	0.0%		
	E_6 (Pa)	1.82×10^{10}	1.0%		

Table 5
Example 5: Investigating the joint inversion performance with respect to the noise level in a bridge comprised of nine piece wisely-homogeneous segments by using NS of 45, GN of 50, and PS of 400: while only the key control parameters are shown in this table, all the stiffness control parameters are visualized in Fig. 19.

Cases	Key Control Parameters	Value	$\mathcal{E}$ (only P, f, E_6)	$\overline{\mathcal{E}}$ (only E_1 to E_9)	$\overline{\mathcal{E}}$
Case 17 Noise level = 0%	P (N/m)	99.66	0.3%	1.0%	0.8%
	f (Hz)	20.00	0.0%		
	E_6 (Pa)	1.82×10^{10}	1.0%		
Case 18 Noise level = 1%	P (N/m)	100.24	0.2%	1.2%	1.0%
	f (Hz)	20.00	0.0%		
	E_6 (Pa)	1.81×10^{10}	0.5%		
Case 19 Noise level = 10%	P (N/m)	100.48	0.5%	2.7%	2.3%
	f (Hz)	20.00	0.0%		
	E_6 (Pa)	1.86×10^{10}	3.3%		
Case 20 Noise level = 20%	P (N/m)	99.67	0.3%	3.8%	3.2%
	f (Hz)	20.04	0.2%		
	E_6 (Pa)	1.97×10^{10}	9.2%		

The parameters used for the GA are NS of 45, GN of 50, and PS of 400. Table 6 shows that the joint inversion successfully estimates the source and structural parameters with an averaged error of 1.5%. Fig. **??** shows the reconstructed E of each segment of the beam. The GA-based optimizer is able to localize the segment with a structural anomaly. Fig. 22 shows the value of the $\overline{\mathcal{E}}$ for the best-fit individual in each generation as the estimated control parameters converge to the their targeted values.

6. Conclusion

We show the feasibility of simultaneously identifying the parameters of the stiffness distribution and a moving vibration source in a Timoshenko beam by using the presented GA-based inverse modeling. We tackle the inverse problem via the minimization of a misfit functional, which is calculated as the difference between sparsely-measured responses induced by target control parameters and their computed counterparts due to estimated parameters.

Table 6
Example 6 - joint inversion of three source parameters and nine stiffness parameters in a bridge comprised of nine piece wisely-homogeneous segments by using NS of 45, GN of 50, and PS of 400: while only the key control parameters are shown in this table, all the stiffness control parameters are visualized in Fig. **??**. The first row shows the targeted control parameters of P, f, a, and E_6. The second row shows their reconstructed values, individual error, and averaged error.

Cases	Key Control Parameters	Value	$\mathcal{E}$ (only P,f,a,E_6)	$\overline{\mathcal{E}}$ (only E_1 to E_9)	$\overline{\overline{\mathcal{E}}}$
Target	P (N/m)	100			
	f (Hz)	20			
	a (m/s^2)	3			
	E_6 (Pa)	1.80×10^{10}			
Case 21	P (N/m)	100.24	0.2%	1.7%	1.5%
	f (Hz)	20.00	0.0%		
	a (m/s^2)	2.93	2.2%		
	E_6 (Pa)	1.78×10^{10}	1.4%		

The numerical results suggest the following findings. First, as shown in Example 1, the more sensors are deployed on the beam, the better accuracy of the presented joint inversion is obtained. Second, Example 1 (i.e., Cases 1 vs 2), Example 3 (i.e., Cases 11 to 13), and Example 4 (i.e., Cases 14 to 17) show that a larger value of PS leads to a better convergence of estimated parameters toward their targeted parameters, while the computational cost of the entire GA process is proportional to the multiplication between GN and PS. Third, as shown in Example 4, in order to successfully invert for the material properties of a beam with a large number of segments, a large value of PS should be used. Fourth, we note that the inversion performance is not sensitive to noise when a small number of control parameters (i.e., five control parameters in Example 2) are estimated. However, as the number of control parameters increases to eleven (i.e., Example 5), the noise affects the inversion performance: the detrimental effect of noise in measurement on the inversion accuracy becomes more significant as the number of control parameters increases. Fifth, it is feasible to conduct the present joint identification even when the targeted moving source's velocity is not constant over time (i.e., Examples 3 and 6).

The present work is limited to structures, of which members' vibrational behaviors are governed by a 1D beam model. The authors, though, note that the present joint inversion method could be applied to various types of structures in a 3D setting as well. For instance, we can apply the presented inverse modeling to a complex bridge structure that should be modeled by 3D cubic or tetrahedral elements. For such an extension, we only need to replace the presented forward wave solver with a new wave solver that is built by using 3D cubic or tetrahedral elements and considering its top surface subject to moving dynamic traction. Such an extension would be onerous but feasible.

6.1. Extensions

In the future, we will extend the presented joint inversion as follows. First, we will extend this 1D beam model into a 3D model so that 3D wave responses of a realistic, detailed bridge model will be taken into account for the inverse modeling. Second, by using the adjoint equation-based approach, we could identify a much larger number of control parameters than those presented in this paper. That is, the material property of each element in the finite element mesh of the 3D model can be inverted for by using the adjoint equation-based material tomography [8]. While the presented GA-based joint inversion method is limited to detecting the material properties of the segments of a piece wisely homogeneous beam model, the adjoint equation-based material tomography could lead to the material inversion performance of a higher resolution than the presented GA-based inversion method. At the same time, the arbitrary profile of moving sources can be identified by using the adjoint equation-based source-reconstruction approach. Recently, Lloyd and Jeong [24] and Guidio and Jeong [10] show that the arbitrarily-varying spatial and temporal distributions of wave source functions can be identified by using the adjoint equation-based source-inversion approach in the 1D and 2D scalar wave settings. As the advantage of the potential adjoint equation-based joint inversion method, due to its semi-analytical nature, its computational cost is small (compared to the GA-based joint inversion) and does not depend on the number of control parameters that are to be identified. In addition, by virtue of the adjoint equation-based joint inversion approach, the spatial function of an estimated wave source profile—i.e., $H(x,t)$ in this work—would not need to be limited to that of a single contact area where traction is applied as the Gaussian distribution. Namely, multiple contact areas of multiple moving wave sources of an arbitrary number and arbitrary traction distributions could be detected under the new adjoint equation-based joint inversion approach.

In a typical material inversion, adding regularization in the objective functional is known to improve the performance of the inversion. For instance, the Tikhonov (TN) regularization could help the numerical optimizer converge to the global minimum of an objective functional while a material discontinuity (a sharp spatial change of a material profile) is suppressed so that an estimated material profile could be smoother than the case for not using the TN regularization. While we invert for E of each finite element by using the new adjoint equation-based joint inversion approach, the targeted profile of E could be recovered by minimizing both the objective functional $\mathcal{L}$ and the TN regularization term $\int_0^L R\left(\frac{\partial E}{\partial x}\right)^2 \mathrm{d}x$, where R is a regularization coefficient. In such a case, although the sharp discontinuity of E around a strong scatterer (anomaly) could be suppressed, the overall spatial distribution of reconstructed E would recover its targeted profile. Besides, the total variation (TV) regularization could be an alternative because it is known to preserve the sharp discontinuity of an estimated material profile while addressing the solution multiplicity of a material inversion problem as well. Thus, the performance of the new adjoint equation-based joint inversion approach aided by each regularization type (e.g., TN vs. TV) shall be investigated in the future.

Lastly, the presented theoretical work and its extensions in the 3D setting under the adjoint-equation-based joint inversion approach should be validated by using real data. To this end, first, we could generate experimental data in a lab setting where a wave source is moving on a beam. To take into account the smaller scale of a lab experimental setup than a realistic bridge, the order of magnitude of the vibration frequency of a target wave source in the lab setting should be higher than that considered in this work. Second, we can validate the 3D extension of our joint inversion modeling by using field data from real bridges.

Acknowledgment

This material is based upon work supported by the National Science Foundation under Award No. CMMI-1855406. Any opinions, findings, and conclusions or recommendations expressed in this material are those of the authors and do not necessarily reflect the views of the National Science Foundation. The authors are very grateful to Dr. Pranav Karve for providing the numerical data of the wave response from his research code for the verification of the presented FEM wave solver. The authors are also grateful to the reviewers, who provided the authors with constructive feedback.

Symbol	Comment
x	Location in a beam
L	Total length of a beam
t	Time
T	Total observation time
$w(x,t)$	Vertical deflection of a beam
$\psi(x,t)$	Slope of a beam caused by bending only
E, G	Elastic and shear moduli
ρ	Mass density
A, I	Cross-sectional area and the second moment of inertia
K_s	Timoshenko shear factor
$q(x,t)$	Vibrational force
s	Location of either a hinge or a roller of a beam
$F(t)$	Temporal variation of $q(x,t)$
$H(x,t)$	Time-dependent (i.e., moving) spatial variation of $q(x,t)$
P, f	Amplitude and frequency of $F(t)$ in $q(x,t)$
x_0	Initial position of $H(x,t)$ in $q(x,t)$ at $t=0$
ϑ	Moving speed of $H(x,t)$ in $q(x,t)$
a	Acceleration of $H(x,t)$ in $q(x,t)$
$u(x)$, $v(x)$	Test functions
$\mathbf{u}$, $\mathbf{v}$	Vectors of nodal solution of test functions
$\mathbf{w}(t)$, $\mathbf{\Psi}(t)$	Vectors of nodal solutions of deflections and slopes
$\boldsymbol{\phi}(x)$, $\mathbf{g}(x)$	Vectors of global basis functions
$\boldsymbol{\phi}'(x)$, $\mathbf{g}'(x)$	Derivatives of vectors of global basis functions with respect to x
M, K	Global mass and stiffness matrices
Q	Global load vector
$\mathbf{d}(t)$	Solution vector composed by $\mathbf{w}(t)$ and $\mathbf{\Psi}(t)$
$\dot{\mathbf{d}}(t)$, $\ddot{\mathbf{d}}(t)$	First- and second-order derivatives of solution vector with respect to t
i	The i-th time step
Δt	Size of time step
$\mathcal{L}$	Objective functional to be minimized
NS	Number of sensors
j	The j-th sensor
$w_j^{\mathsf{m}}(t)$	Measured response at the location of the j-th sensor and time t
$w_j(t)$	Computed response at the location of the j-th sensor and time t
GN, PS	Number of generations and population size
$\mathcal{E}$	Error between a target control parameter and its estimated solution
$\overline{\mathcal{E}}$	Averaged error norm for all the control parameters
NP	Total number of target control parameters
k	The k-th control parameter
E_n	The Elastic modulus of each n-th segment of the beam

393 # 7. Nomenclature

References

[1] Akcelik, V., Biros, G., Ghattas, O., 2002. Parallel multiscale Gauss-Newton-Krylov methods for inverse wave propagation, in: Supercomputing, ACM/IEEE 2002 Conference, IEEE. pp. 41–41.

[2] Akula, V.R., Ganguli, R., 2003. Finite element model updating for helicopter rotor blade using genetic algorithm. AIAA Journal 41, 554–556. URL: https://doi.org/10.2514/2.1983, doi:10.2514/2.1983, arXiv:https://doi.org/10.2514/2.1983.

[3] Caglar, N.M., Safak, E., 2019. Application of spectral element method for dynamic analysis of plane frame structures. Earthquake Spectra 35, 1213–1233. URL: https://doi.org/10.1193/050818EQS115M, doi:10.1193/050818EQS115M.

[4] Cavadas, F., Smith, I.F., Figueiras, J., 2013. Damage detection using data-driven methods applied to moving-load responses. Mechanical Systems and Signal Processing 39, 409 – 425. URL: http://www.sciencedirect.com/science/article/pii/S0888327013000988, doi:https://doi.org/10.1016/j.ymssp.2013.02.019.

[5] Choi, H., Popovics, J.S., 2015. NDE application of ultrasonic tomography to a full-scale concrete structure. IEEE Transactions on Ultrasonics, Ferroelectrics, and Frequency Control 62, 1076–1085. doi:10.1109/TUFFC.2014.006962.

[6] Du, C., Dutta, S., Kurup, P., Yu, T., Wang, X., 2019. A review of railway infrastructure monitoring using fiber optic sensors. Sensors and Actuators A: Physical , 111728URL: http://www.sciencedirect.com/science/article/pii/S0924424719309483, doi:https://doi.org/10.1016/j.sna.2019.111728.

[7] Eshkevari, S.S., Pakzad, S.N., Takac, M., Matarazzo, T.J., 2020. Modal identification of bridges using mobile sensors with sparse vibration data. Journal of Engineering Mechanics 146, 04020011. doi:10.1061/(ASCE)EM.1943-7889.0001733.

[8] Fathi, A., Kallivokas, L.F., Poursartip, B., 2015. Full-waveform inversion in three-dimensional PML-truncated elastic media. Computer Methods in Applied Mechanics and Engineering 296, 39–72.

[9] Fathi, A., Poursartip, B., Stokoe II, K.H., Kallivokas, L.F., 2016. Three-dimensional P-and S-wave velocity profiling of geotechnical sites using full-waveform inversion driven by field data. Soil Dynamics and Earthquake Engineering 87, 63–81.

[10] Guidio, B., Jeong, C., 2020. Full-waveform inversion of incoherent dynamic traction in a bounded 2D domain of scalar wave motions. Journal of Engineering Mechanics (under review) .

[11] Guzina, B.B., Fata, S.N., Bonnet, M., 2003. On the stress-wave imaging of cavities in a semi-infinite solid. International Journal of Solids and Structures 40, 1505–1523.

[12] Jeong, C., Na, S.W., Kallivokas, L.F., 2009. Near-surface localization and shape identification of a scatterer embedded in a halfplane using scalar waves. Journal of Computational Acoustics 17, 277–308.

[13] Jeong, C., Seylabi, E.E., 2018. Seismic input motion identification in a heterogeneous halfspace. Journal of Engineering Mechanics 144, 04018070. doi:10.1061/(ASCE)EM.1943-7889.0001495.

[14] Jung, J., Jeong, C., Taciroglu, E., 2013. Identification of a scatterer embedded in elastic heterogeneous media using dynamic XFEM. Computer Methods in Applied Mechanics and Engineering 259, 50–63.

[15] Jung, J., Taciroglu, E., 2014. Modeling and identification of an arbitrarily shaped scatterer using dynamic XFEM with cubic splines. Computer Methods in Applied Mechanics and Engineering 278, 101–118.

[16] Kallivokas, L.F., Fathi, A., Kucukcoban, S., Stokoe, K.H., Bielak, J., Ghattas, O., 2013. Site characterization using full waveform inversion. Soil Dynamics and Earthquake Engineering 47, 62–82.

[17] Kang, J.W., Kallivokas, L.F., 2010. The inverse medium problem in 1D PML-truncated heterogeneous semi-infinite domains. Inverse Problems in Science and Engineering 18, 759–786. doi:10.1080/17415977.2010.492510.

[18] Kang, J.W., Kallivokas, L.F., 2011. The inverse medium problem in heterogeneous PML-truncated domains using scalar probing waves. Computer Methods in Applied Mechanics and Engineering 200, 265 – 283. URL: http://www.sciencedirect.com/science/article/pii/S0045782510002434, doi:https://doi.org/10.1016/j.cma.2010.08.010.

[19] Karve, P.M., Na, S.W., Kang, J.W., Kallivokas, L.F., 2011. The inverse medium problem for Timoshenko beams and frames: damage detection and profile reconstruction in the time-domain. Computational Mechanics 47, 117–136.

[20] Khaji, N., Shafiei, M., Jalalpour, M., 2009. Closed-form solutions for crack detection problem of timoshenko beams with various boundary conditions. International Journal of Mechanical Sciences 51, 667 – 681. URL: http://www.sciencedirect.com/science/article/pii/S0020740309001398, doi:https://doi.org/10.1016/j.ijmecsci.2009.07.004.

[21] Kucukcoban, S., Goh, H., Kallivokas, L.F., 2019. On the full-waveform inversion of Lame parameters in semi-infinite solids in plane strain. International Journal of Solids and Structures 164, 104 – 119. URL: http://www.sciencedirect.com/science/article/pii/S0020768319300289, doi:https://doi.org/10.1016/j.ijsolstr.2019.01.019.

[22] Law, S., Zhu, X., 2000. Study on different beam models in moving force identification. Journal of Sound and Vibration 234, 661 – 679. URL: http://www.sciencedirect.com/science/article/pii/S0022460X00928670, doi:https://doi.org/10.1006/jsvi.2000.2867.

[23] Liu, J., Chen, S., BergAs, M., Bielak, J., Garrett, J.H., Kovacevic, J., Noh, H.Y., 2020. Diagnosis algorithms for indirect structural health monitoring of a bridge model via dimensionality reduction. Mechanical Systems and Signal Processing 136, 106454. URL: http://www.sciencedirect.com/science/article/pii/S0888327019306752, doi:https://doi.org/10.1016/j.ymssp.2019.106454.

[24] Lloyd, F., Jeong, C., 2018. Adjoint equation-based inverse-source modeling to reconstruct moving acoustic sources in a 1D heterogeneous solid. Journal of Engineering Mechanics 144, 04018089. doi:10.1061/(ASCE)EM.1943-7889.0001508.

[25] Lloyd, S., Jeong, C., Nath Gharti, H., Vignola, J., Tromp, J., 2019. Spectral-element simulations of acoustic waves induced by a moving underwater source. Journal of Theoretical and Computational Acoustics 27.

[26] Mehrjoo, M., Khaji, N., Ghafory-Ashtiany, M., 2013. Application of genetic algorithm in crack detection of beam-like structures using a new cracked euler-bernoulli beam element. Applied Soft Computing 13, 867 – 880. URL: http://www.sciencedirect.com/science/article/pii/S1568494612004346, doi:https://doi.org/10.1016/j.asoc.2012.09.014.

[27] Mei, Q., GÃČÅŠl, M., Boay, M., 2019. Indirect health monitoring of bridges using mel-frequency cepstral coefficients and principal component analysis. Mechanical Systems and Signal Processing 119, 523 – 546. URL: http://www.sciencedirect.com/science/article/

pii/S0888327018306678, doi:https://doi.org/10.1016/j.ymssp.2018.10.006.
[28] Newmark, N.M., 1959. A method of computation for structural dynamics. Journal of the Engineering Mechanics Division 85, 67–94.
[29] Pakravan, A., Kang, J.W., Newtson, C.M., 2016. A Gauss-Newton full-waveform inversion for material profile reconstruction in viscoelastic semi-infinite solid media. Inverse Problems in Science and Engineering 24, 393–421. URL: http://dx.doi.org/10.1080/17415977.2015.1046861, doi:10.1080/17415977.2015.1046861.
[30] Sarkar, K., Ganguli, R., 2014. Analytical test functions for free vibration analysis of rotating non-homogeneous timoshenko beams. Meccanica 49, 1469âĂŞ1477. doi:10.1007/s11012-014-9927-8.
[31] Schaal, C., Mal, A., 2016. Lamb wave propagation in a plate with step discontinuities. Wave Motion 66, 177–189. doi:10.1016/j.wavemoti.2016.06.012.
[32] Tran, K.T., McVay, M., 2012. Site characterization using Gauss-Newton inversion of 2-D full seismic waveform in the time domain. Soil Dynamics and Earthquake Engineering 43, 16–24. URL: https://linkinghub.elsevier.com/retrieve/pii/S0267726112001613, doi:10.1016/j.soildyn.2012.07.004.
[33] Waisman, H., Chatzi, E., Smyth, A.W., 2010. Detection and quantification of flaws in structures by the extended finite element method and genetic algorithms. International Journal for Numerical Methods in Engineering 82, 303–328.

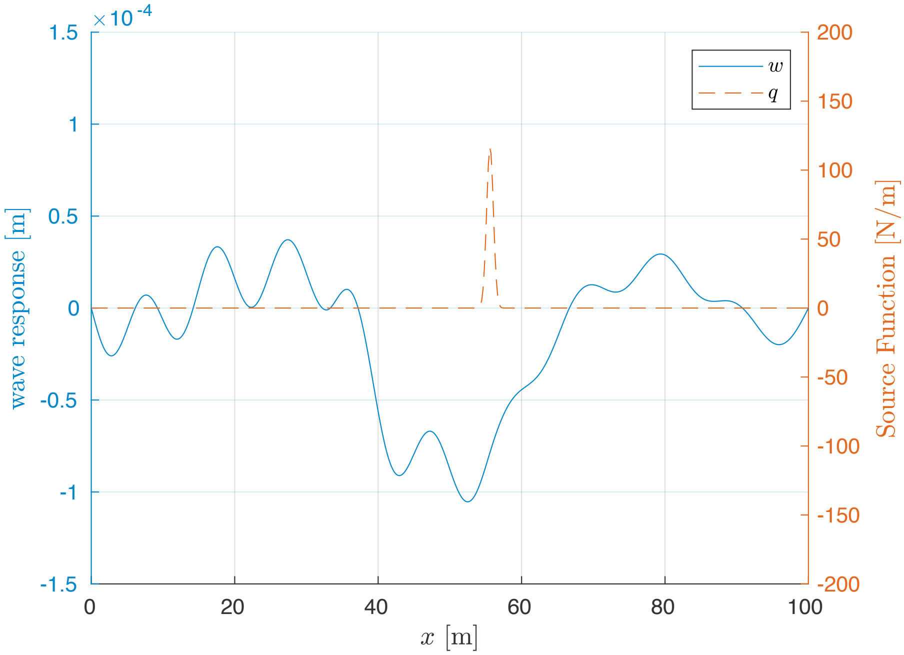

(a) measured at t of 0.28 s

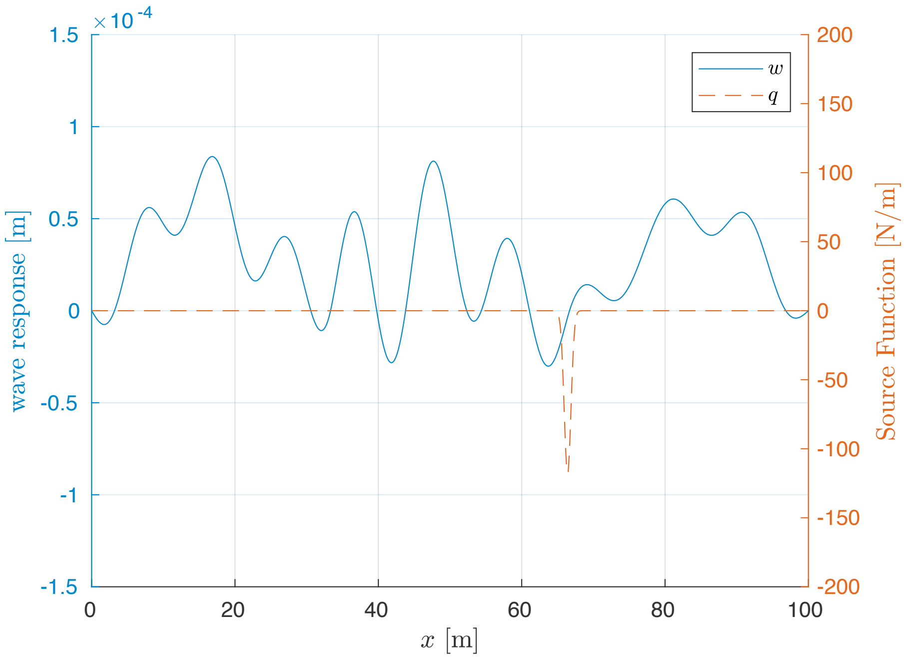

(b) measured at t of 0.82 s

Figure 6: Snapshots of the exemplary wave response, $w(x, t)$, and the targeted source function, $q(x, t)$, in Example 1 considering the targeted material profile.

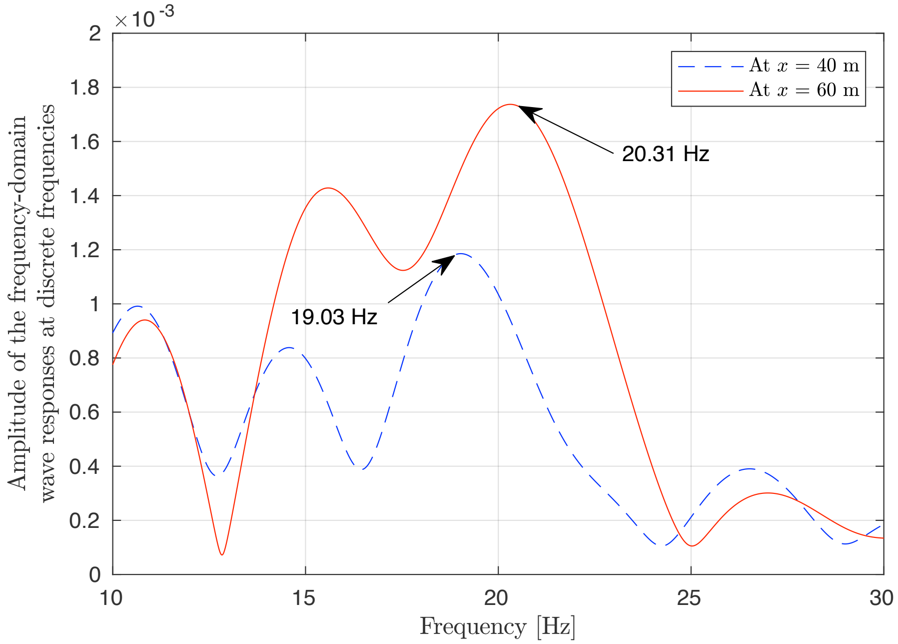

Figure 7: The Doppler effect of the wave responses $w(x, t)$ induced by a moving source in Example 1 considering the targeted material profile.

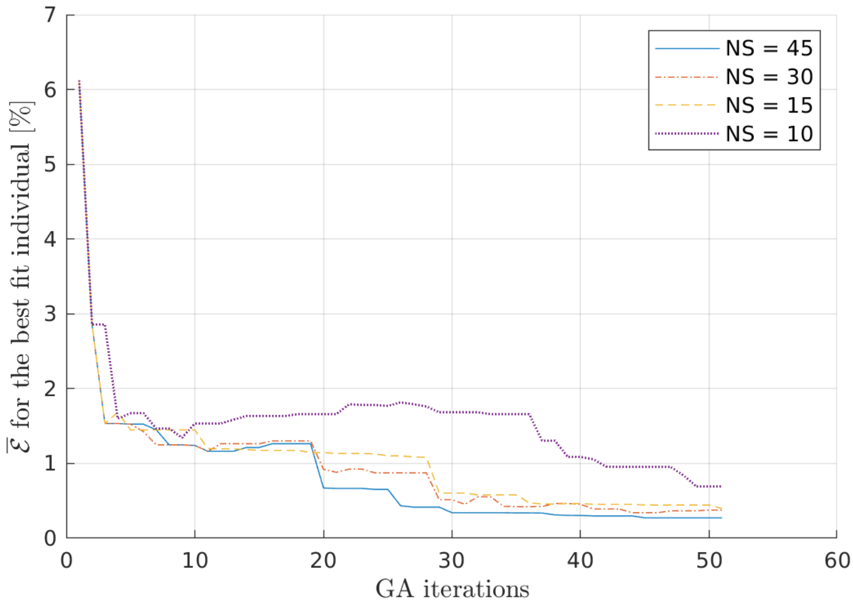

Figure 8: The average error for the best-fit individual versus the GA iterations in Cases 2, 3, 4 and 5 of Example 1.

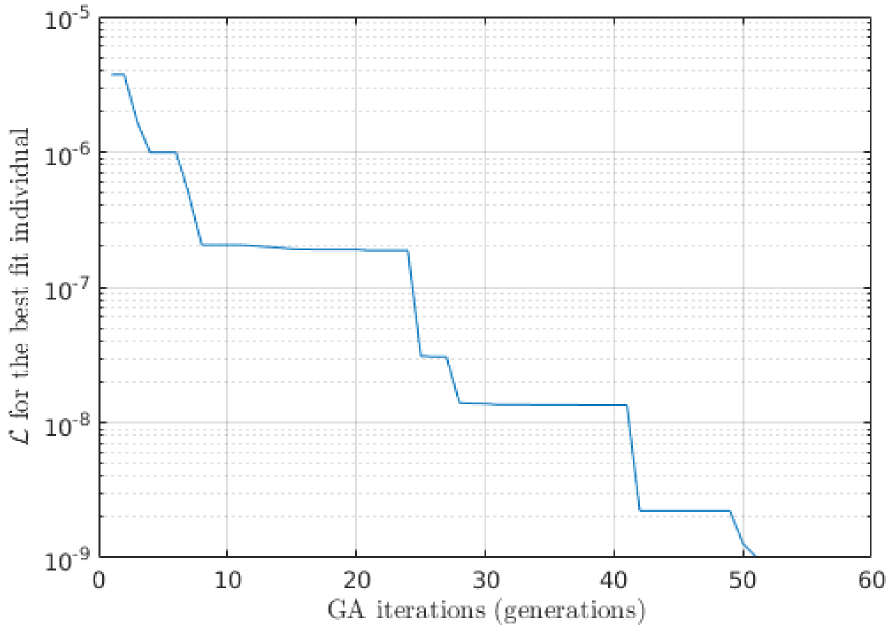

Figure 9: The misfit functional for the best-fit individual over the GA iterations in Case 1.

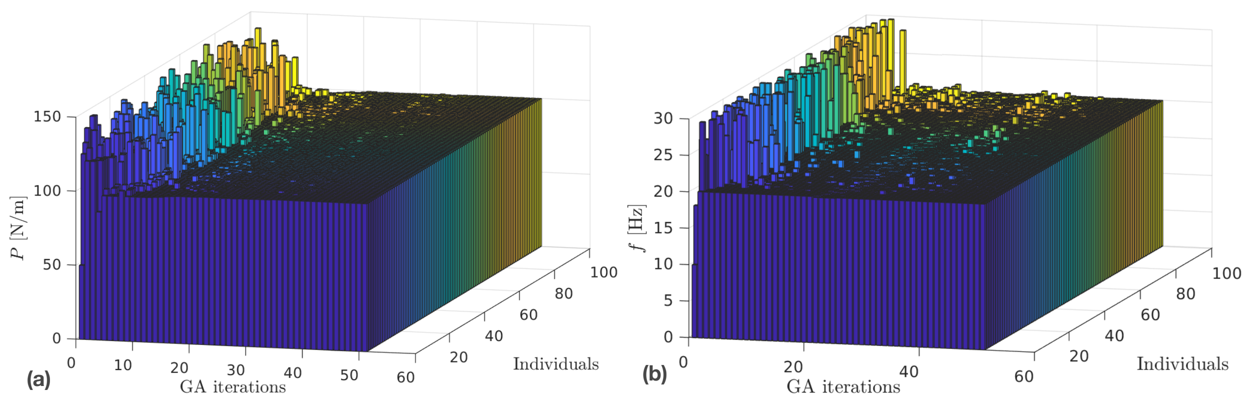

Figure 10: The histograms of (a) P and (b) f of the entire individuals at all the generations in Case 1.

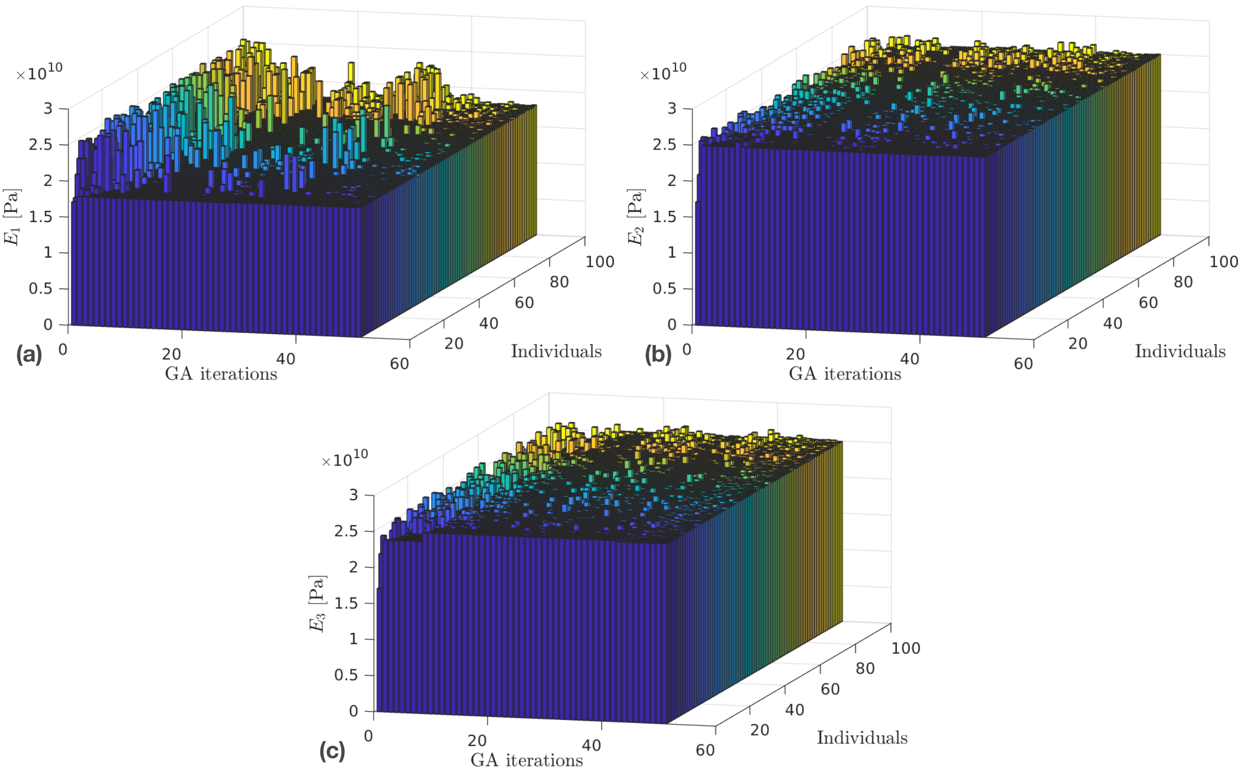

Figure 11: The histograms of (a) E_1, (b) E_2, and (c) E_3 of the entire individuals at all the generations in Case 1.

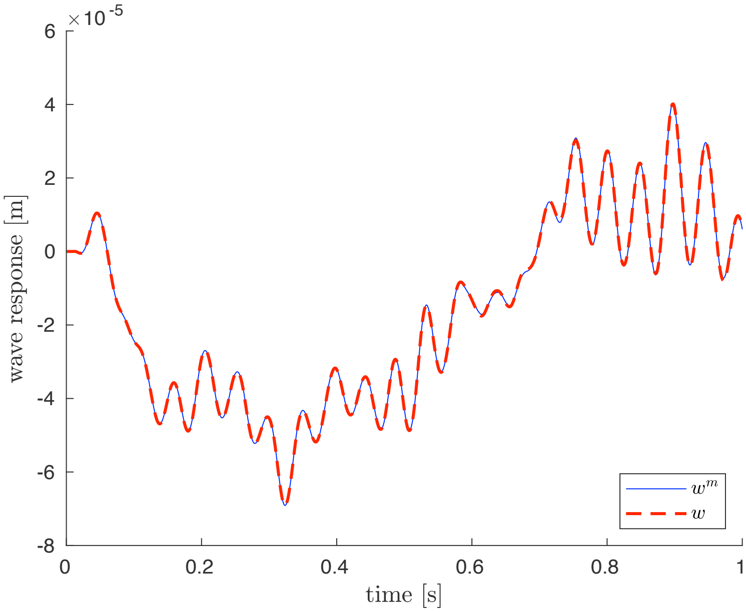

(a) measured at x of 40 m

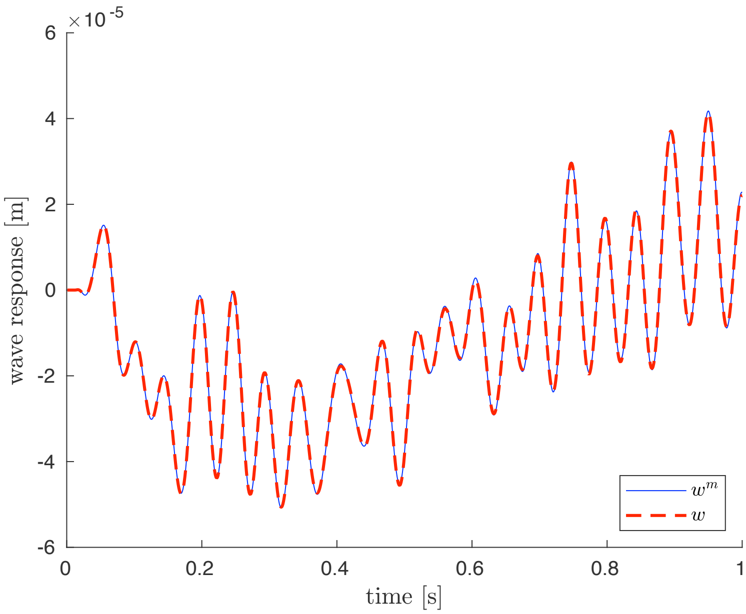

(b) measured at x of 60 m

Figure 12: Wave responses, w^{m} and w, at the sensors in Case 1.

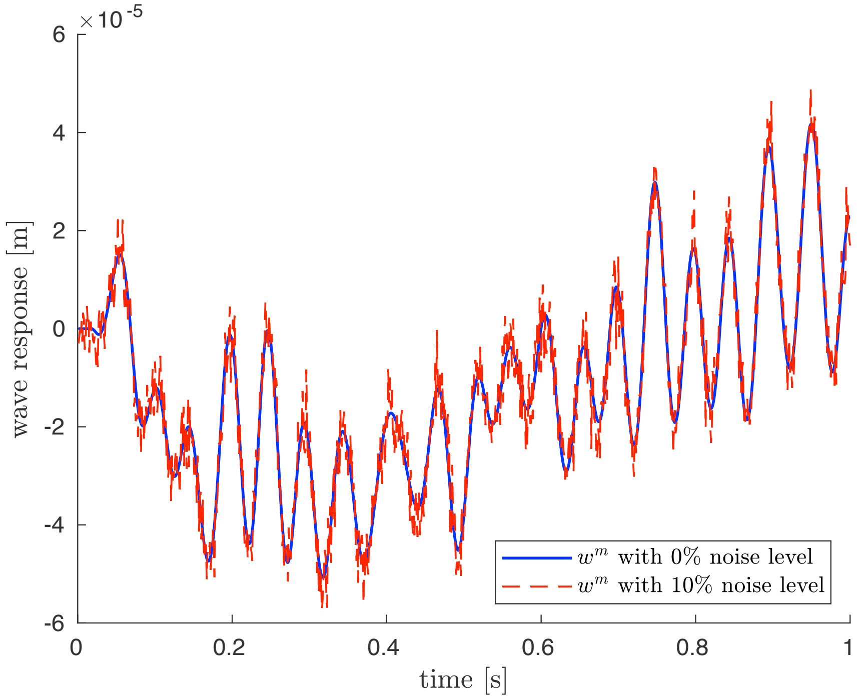

Figure 13: w^m with 0% noise level (Case 1) and w^m with 10% noise level (Case 8) at a sensor at $x = 60$ m in Example 2.

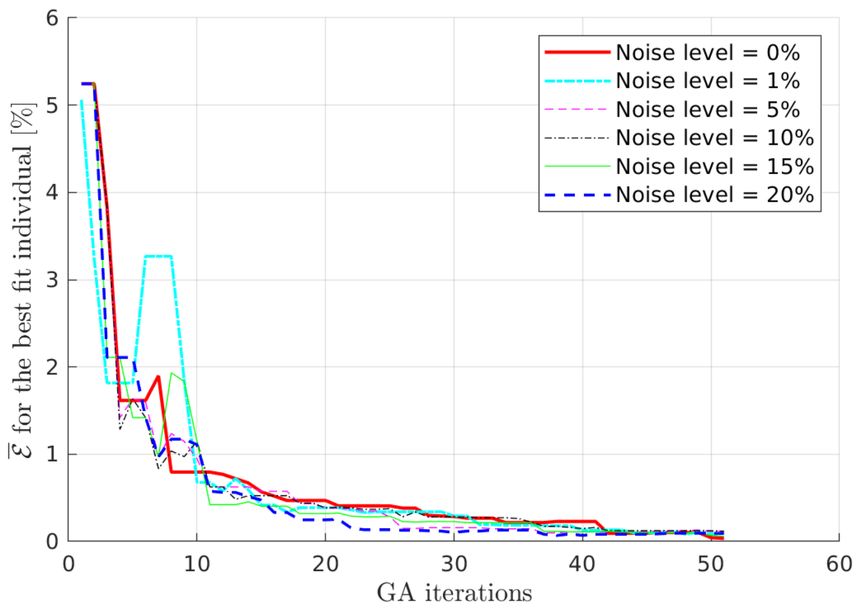

Figure 14: $\overline{\mathcal{E}}$ for the best-fit individual versus the GA iteration in Example 2.

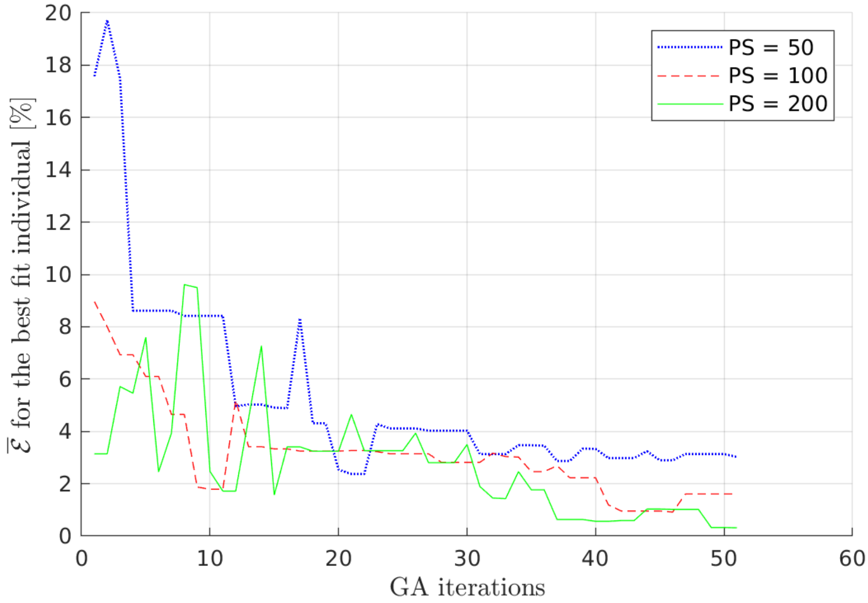

Figure 15: $\overline{\mathcal{E}}$ for the best-fit individual versus the GA iteration in Example 3.

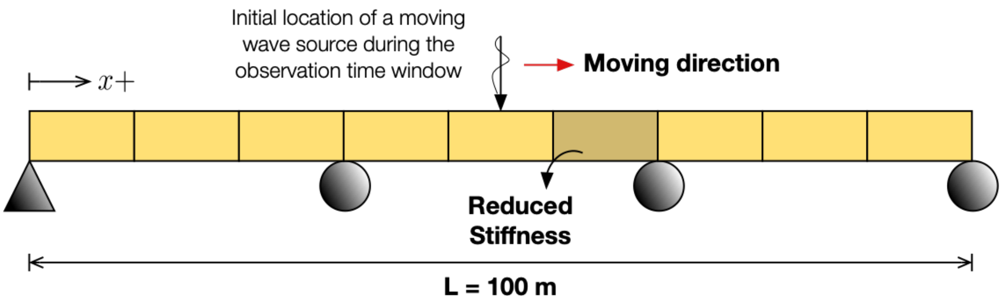

Figure 16: A piece wisely-homogeneous Timoshenko beam with nine segments in Example 4, 5, and 6.

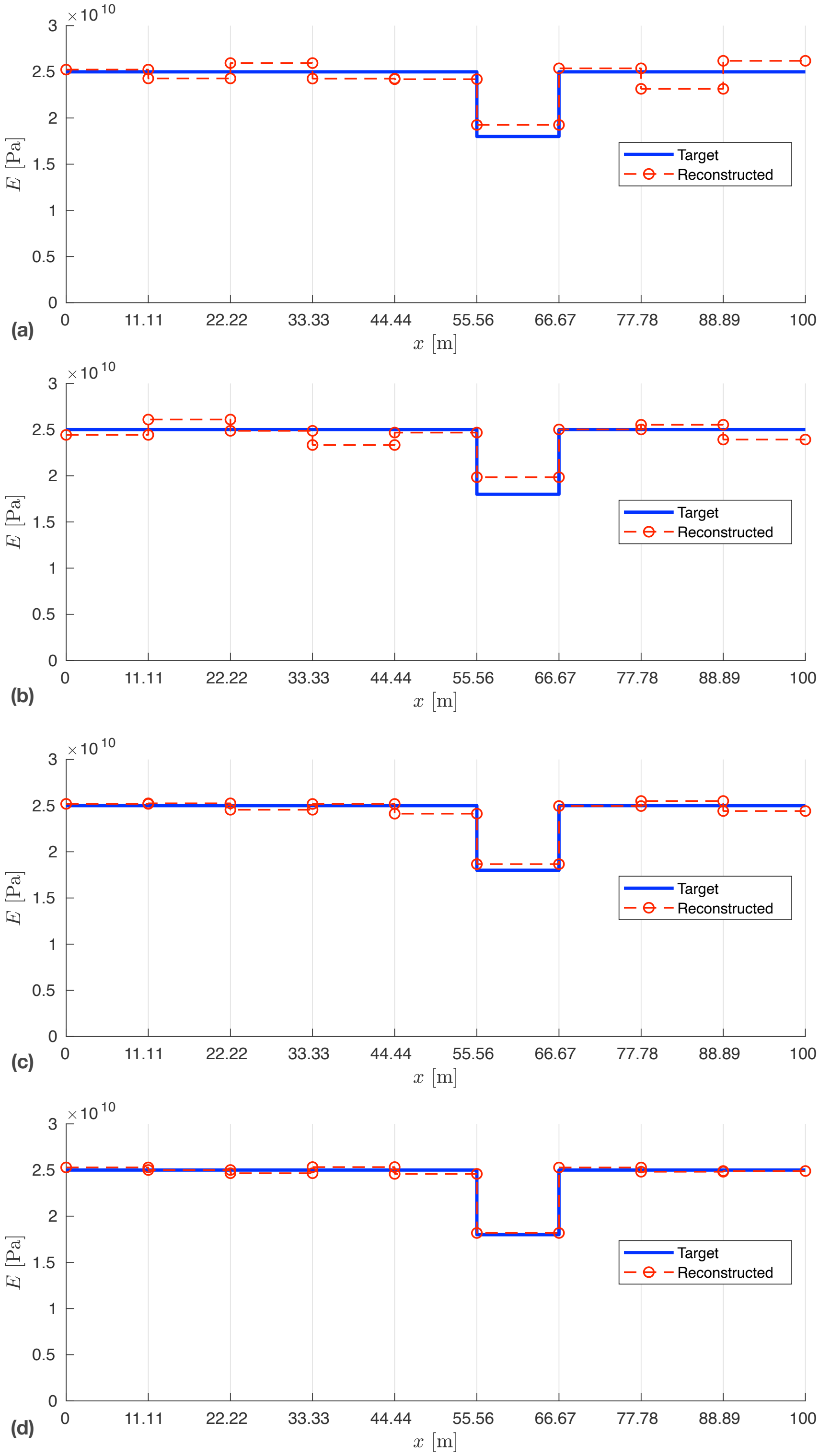

Figure 17: The reconstructed elastic modulus of a piece wisely-homogeneous beam of nine segments via the joint inversion in Example 4: (a) Case 14 using PS of 50, (b) Case 15 using PS of 100, (c) Case 16 using PS of 200, and (d) Case 17 using PS of 400.

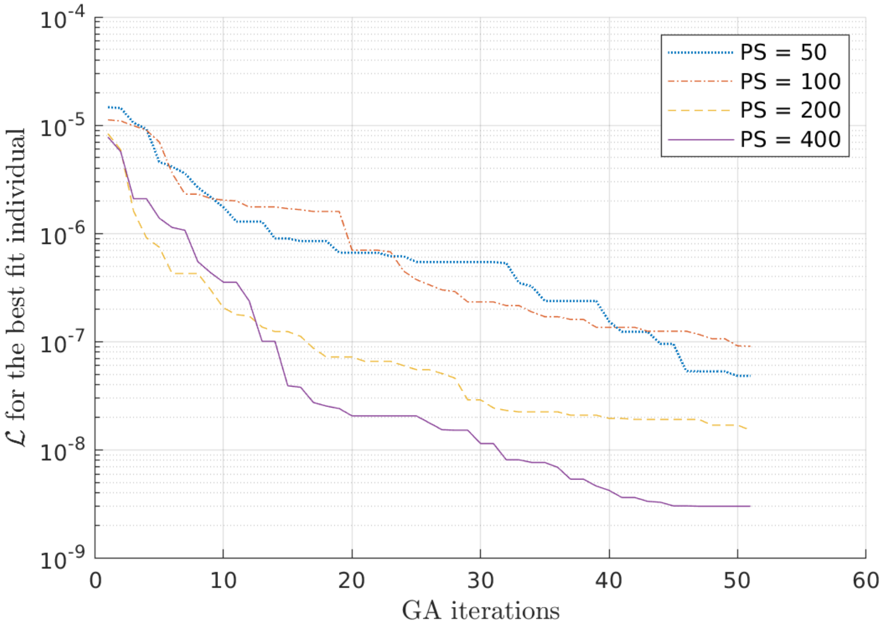

(a) The misfit functional $\mathcal{L}$

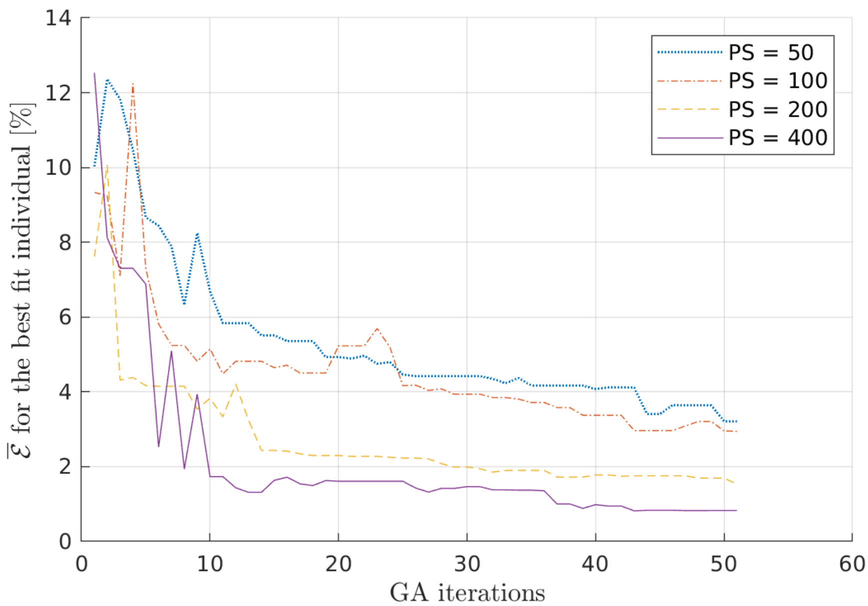

(b) The average error $\overline{\mathcal{E}}$

Figure 18: (a) $\mathcal{L}$ and (b) $\overline{\mathcal{E}}$ for the best-fit individual versus the GA iteration in Example 4.

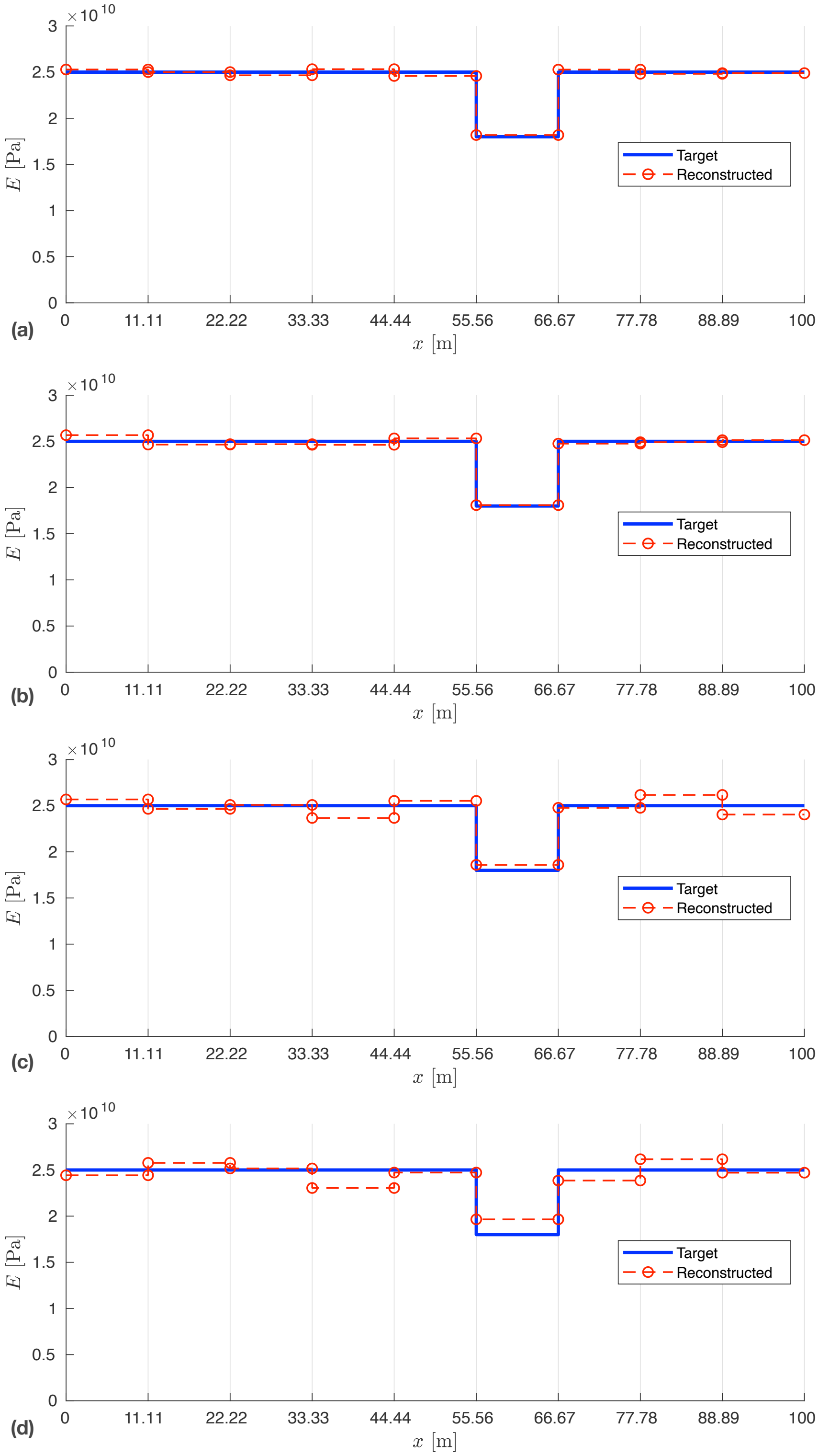

Figure 19: The reconstructed elastic modulus of a piece wisely-homogeneous beam of nine segments via the joint inversion in Example 5: (a) Case 17 using Noise level of 0%, (b) Case 18 using Noise level of 1%, (c) Case 19 using Noise level of 10%, and (d) Case 17 using Noise level of 20%.

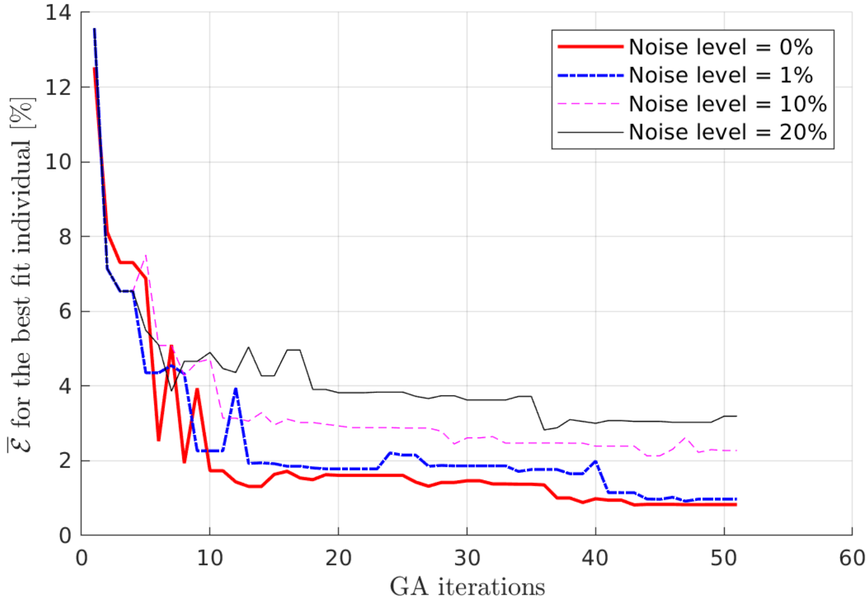

Figure 20: $\overline{\mathcal{E}}$ for the best-fit individual versus the GA iteration in Example 5.